Title
THE ELASTIC SCATTERING OF 5-BEV n- MESONS OK HYDROGEN

Author
Thomas, Richard Garland

Publication Date
1959-11-03

UCRL 8965

UNIVERSITY OF CALIFORNIA

Ernest O. Lawrence Radiation Laboratory

BERKELEY, CALIFORNIA

DISCLAIMER

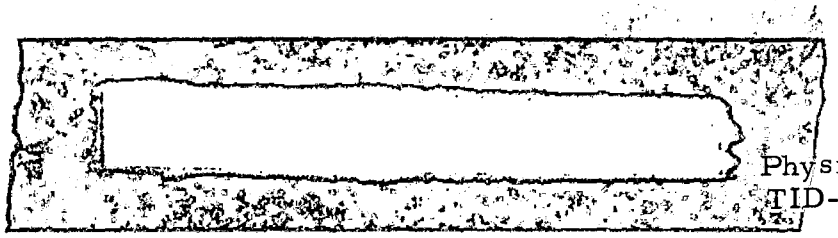

UCRL-8965
Physics and Mathematics
TID-4500 (15 ed.)

UNIVERSITY OF CALIFORNIA
Lawrence Radiation Laboratory
Berkeley, California

Contract No. W-7405-eng-48

THE ELASTIC SCATTERING OF 5-BEV π^- MESONS ON HYDROGEN

Richard Garland Thomas, Jr.
(Thesis)

November 3, 1959

Printed for the U. S. Atomic Energy Commission

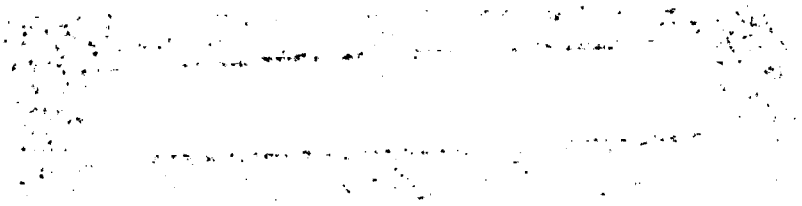

Printed in USA. Price $1.75. Available from the
Office of Technical Services
U. S. Department of Commerce
Washington 25, D.C.

THE ELASTIC SCATTERING OF 5-BEV π^- MESONS ON HYDROGEN

Contents

Abstract	3
I. Introduction	4
II. Experimental Techniques	6
Beam Geometry	6
The Bubble Chamber	6
Pion Beam	12
Scanning	16
Acceptance Criteria for Events and Pictures	18
III. Measurement	25
IV. Identification of Events	27
V. Discussion of Errors	32
Momentum Errors	34
Angle Errors	34
VI. Corrections to the Observed Data	
Scanning Efficiency	38
Background Events	38
Orientation of the Scattering Plane	47
Location of Events in the Chamber	47
Mu Contamination	49
VII. Results and Conclusions	
Angular Distribution	50
Total Elastic Cross Section	57
Acknowledgments	59
Appendix: Modified Least-Squares Procedure for the Angular Distribution	60
References	62

THE ELASTIC SCATTERING OF 5-BEV π^- MESONS ON HYDROGEN

Richard Garland Thomas, Jr.

Lawrence Radiation Laboratory
University of California
Berkeley, California

November 3, 1959

ABSTRACT

The results of the elastic scattering of 5-Bev negative pions on hydrogen are reported in detail. A description of the propane bubble chamber is given. Two different methods of identification of events are described, and the errors that limit the accuracy of each considered. Particular attention is directed to the problem of background events. It is shown that $\sim 7 (\pm 3)\%$ of the events called elastic are background. The data are analyzed in terms of the optical model because the angular distribution shows the sharp rise in the forward direction characteristic of diffraction scattering. The modified least-squares procedure used to fit the data is outlined. From the least-squares representation of the best-fitting curve, it is found that $\frac{d\sigma\ (0)}{d\omega} = 29.8$ mb/sterad in the center-of-mass system, and the pion radius of the proton is $1.04 \pm 0.05 \times 10^{-13}$ cm. The total elastic cross section is 5.6 ± 0.5 mb. The results are compared with those derived from theory and other experiments. It is shown that the assumption that the proton acts like a black sphere leads to an elastic cross section much higher than observed. From the above value of the differential cross section in the forward direction, the total hydrogen cross section is found to be 29.1 ± 2.9 mb. This leads to a value for the opacity of the sphere of 0.69 ± 0.05.

I. INTRODUCTION

Since the discovery that pi mesons interact strongly with nucleons,[1] much time has been and is currently being spent studying these interactions. It is now fairly certain that when a satisfactory theory of nuclear forces is enunciated, the pions will play a dominant role. Among the many interactions of pions with protons at moderate energies ($\leq$ 1 Bev), elastic scattering can be studied most readily. The information that is obtained in one of these experiments usually consists of:

(a) the pion size of the proton

(b) the angular distribution of the elastically scattered mesons

(c) a test of one or more models of the nucleus

(d) the total elastic scattering cross section.

The pion size of the proton is known to be of the order 10^{-13} cm, but the question of whether the values reported in the past[2,3,4] represent real differences or just experimental errors remains to be answered. Also to be determined is the connection between the various sizes--e.g., pion size, proton size,[5,6,7] etc.--and how these are related, if at all, to the electron size.[8]

The angular distribution of the elastically scattered mesons is observed to undergo rather noticeable changes in the backward hemisphere (center-of-mass system) in the energy region $500 \leq E_\pi \leq 1000$ Mev. In the forward hemisphere the distribution, which at low energies is the result of nondiffraction potential scattering, results in large part from diffraction scattering at $\sim$ 1.5 Bev.

As the nature of the elastic interaction changes, so also do the models used to describe it. Partial-wave analysis,[9] which is adequate at low energies where the number of angular momentum states is small, becomes unwieldy in the Bev region. In the latter region the description of the process has paralleled that used in classical physical optics. As the energy of the incident pion increases, the elastic cross section is observed to drop steadily as processes involving multiple meson production and strange-particle production become more important.[10]

The rate of accumulation of data on pion interactions has increased greatly since the invention of the bubble chamber[11] primarily because of the increase in density of material. The experiment that is to be described was performed in one of the largest bubble chambers presently in existence. The purpose of the run was to study pion interactions in general, and this report covers only the elastic scattering interaction. The results of studies of the Λ and Ξ^- hyperons have already been reported.[12, 13]

II. EXPERIMENTAL ARRANGEMENT OF APPARATUS

Beam Geometry

The geometry of the beam is shown in Fig. 1. A beryllium target was plunged periodically into the path of the circulating proton beam along a radius 14 degrees (deg) upstream from a radius through the center of the west straight section of the Bevatron.

Negative pions emitted at zero degrees to the proton beam were deflected 29.95 deg from this beam through a thin window in the vacuum tank. They then passed successively through two standard 8-in. quadrupole triplets each of which was operated as a single lens. A 5-ft analyzing magnet having a 7-in. gap then bent the mesons through 7.2 deg into the position occupied by the 30-in. propane bubble chamber. The total distance from the target to the center of the chamber was 56 ft.

The Bubble Chamber

The 30-in. propane bubble chamber, which has been described previously,[14] is shown in Fig. 2. Shaped like an oval, it has a sensitive volume of 30-1/2 by 21-1/2 by 6-1/2 in. The chamber is made of 1/8-in. stainless steel throughout except for the top and bottom glasses which are each 3/8-in. thick.

This instrument normally operates at a temperature of 60 to 61°C and a pressure of 390 pounds per square inch (psi). A steel tank 62 in. high and filled with mineral oil encloses the chamber. The oil serves as a hydrostatic support, permitting high-pressure operation with relatively thin glass windows.

Expansion and compression of the propane is achieved through the operation of eight Barksdale valves mounted symmetrically round the outer circumference of the tank near the top. Through these valves nitrogen gas at 390 psi flows onto a Hycar rubber diaphragm mounted around the inner circumference of the tank. Resulting expansion of the diaphragm compresses the oil which, in turn, compresses the propane through the vertical motion of the top glass, which is flexibly mounted on another Hycar rubber diaphragm. This diaphragm is held to the side walls of the chamber by a clamping ring. Expansion of the chamber

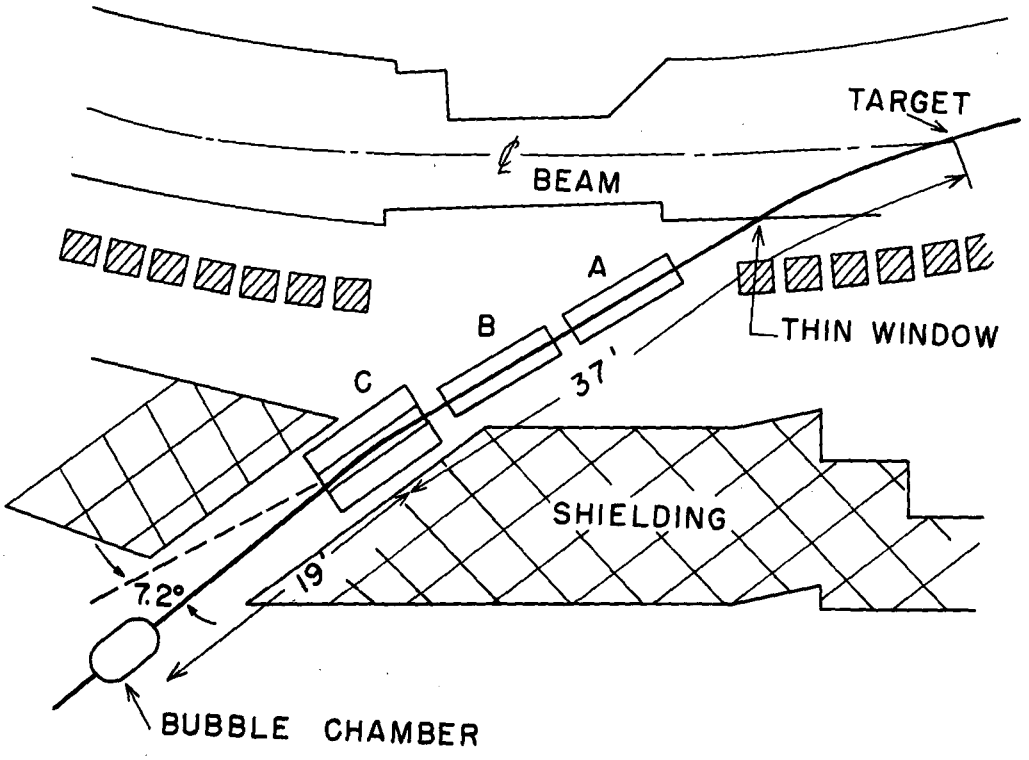

Fig. 1. The beam geometry.

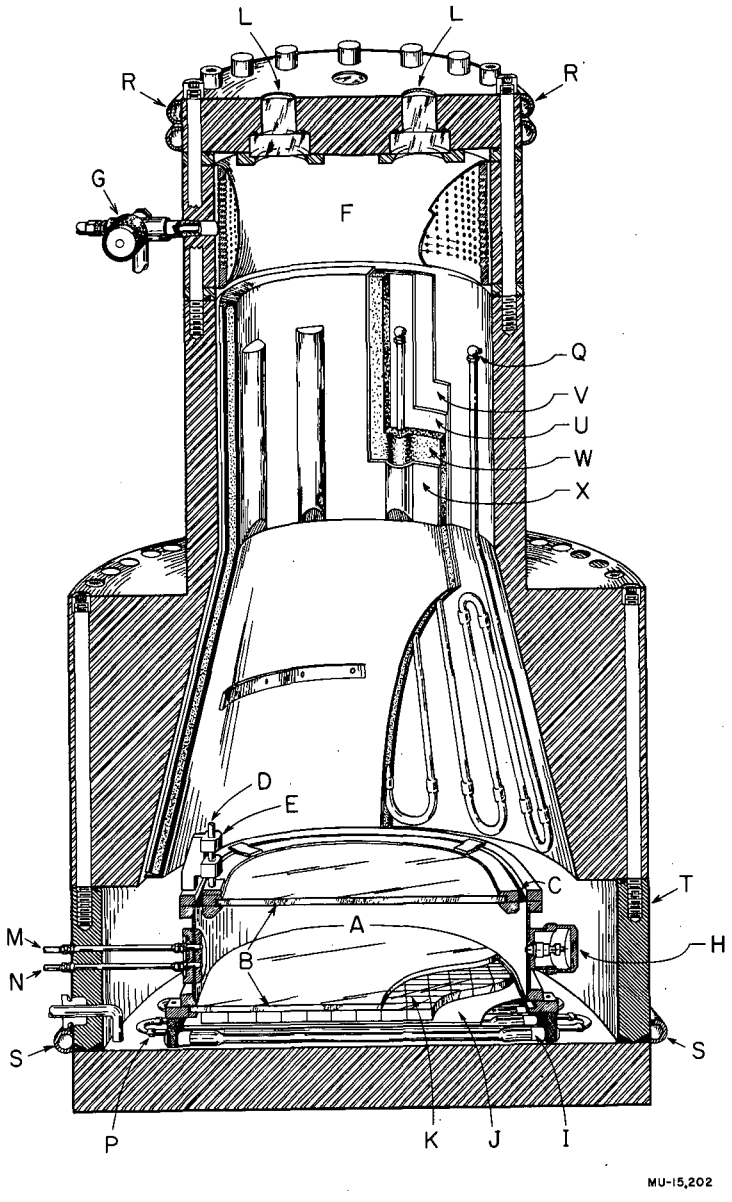

Fig. 2. The 30-inch propane bubble chamber, showing (a) the propane container, (b) the glass windows, (c) flexible rubber diaphragm between side wall and top-glass clamping ring, (d) stainless steel guiding rod, (e) cylindrical ball bearings controlling the guiding rod, (f) cylindrical Hycar rubber diaphragm, (g) 3/4-in. Barksdale valve, (h) transducer for measuring the propane pressure, (i) one of the 13 flash tubes, (j) opal-glass diffuser, (k) venetian-blind light collimator, (l) two of the four viewing ports in the top of the chamber, (m) thermocouple for measuring the propane temperature, (n) propane fill tube, (p) water tubes under the chamber, (q) water tubes in the upper part of the oil container, (r) water tube around the top cover plate, (s) water tube around the bottom of the oil container, (t) nonmagnetic steel region, (u) copper sheet, (v) Mylar sheet, (w) polyurethane sponge, and (x) copper sheet.

forces the nitrogen into a tank containing the gas at 5 psi. The chamber is fully expanded after 45 milliseconds (msec) and recompresses in about the same time. The top glass moves about 0.2 in.

The operation of the chamber results in a sensitive time of at least 4 msec, and the lights are flashed from 2 to 6 msec after the arrival of the beam. The Bevatron is pulsed 10 times per minute. Prior to the arrival of a pulse an electrical signal from the control room of the accelerator actuates the various delay circuits that control the expansion mechanism, the flashing of the lights, and the recompression mechanism.

Nuclear interactions within the sensitive volume are photographed from the top of the outer pressure vessel through two 2-in. -diam. glass windows; these windows are 1-1/2 in. thick. Light from 13 flash tubes beneath the chamber passes through a "venetian blind", which directs the light entering the chamber away from the two viewing ports, so that the bubbles appear against a dark background. This blind consists of strips of lucite 3/4-in. wide and 1/16-in. thick. These strips, tilted at an angle of 20 deg from the viewing ports and cemented together, form a solid, 3/4-in. -thick sheet that covers the bottom of the chamber.

The apparatus is brought to and maintained at operating temperature by hot water circulating through two separate sets of copper tubes. One set is mounted between the lights along the bottom of the tank, while the other runs around its upper perimeter.

Figure 3 shows the chamber in the large magnet that is designed to provide a steady magnetic field of 13,500 gauss over the volume of the propane.[14] In Fig. 4 we show the console for over-all control of the operation of the apparatus.

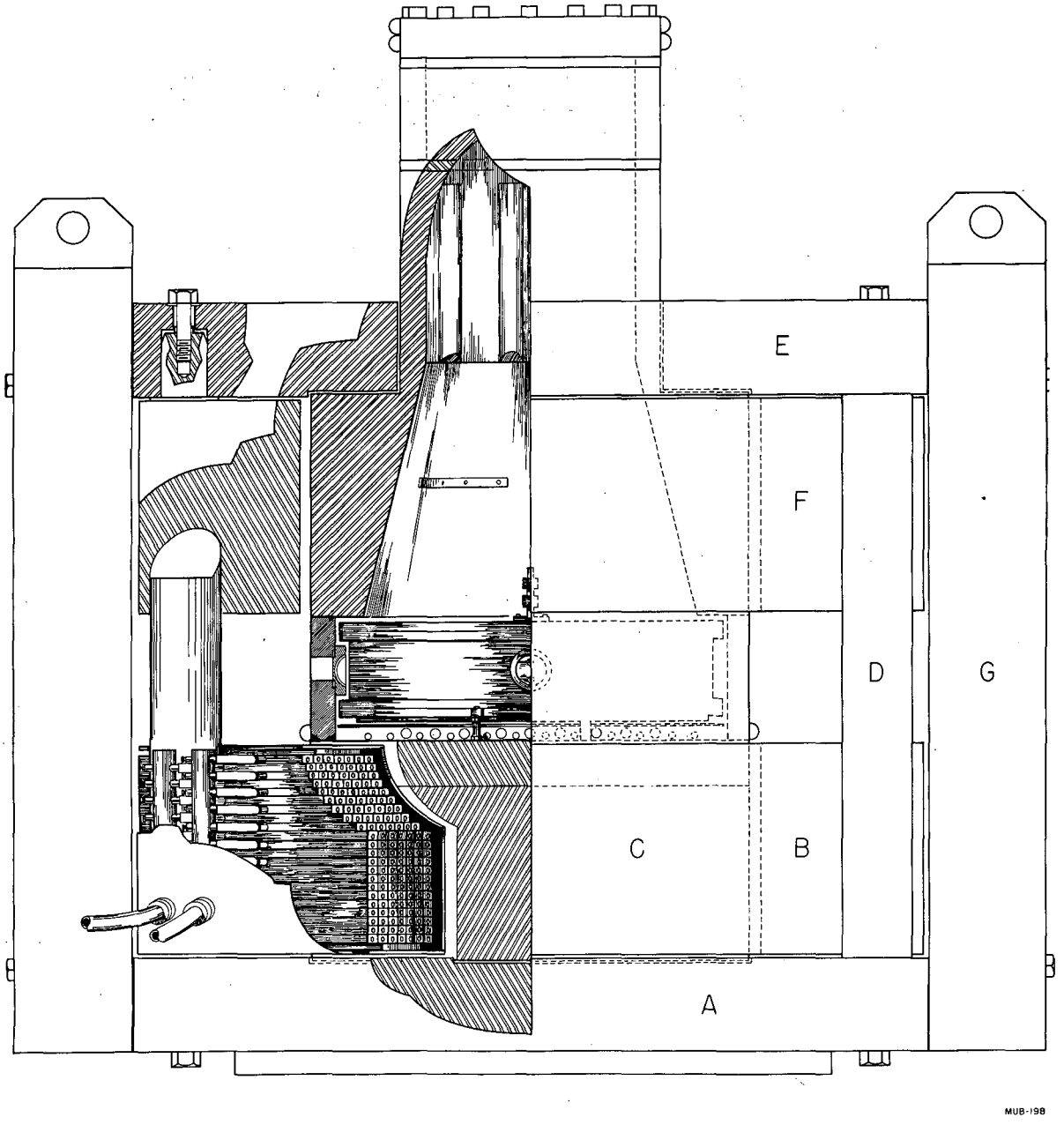

Fig. 3. The 30-inch propane bubble chamber in its magnet, showing (a) iron slab forming the bottom of the magnet, (b) bottom copper coil, (c) iron cylinder, (d) four iron posts supporting top slab E, (e) upper iron slab, (f) upper coil of the magnet, and (g) magnetic return path.

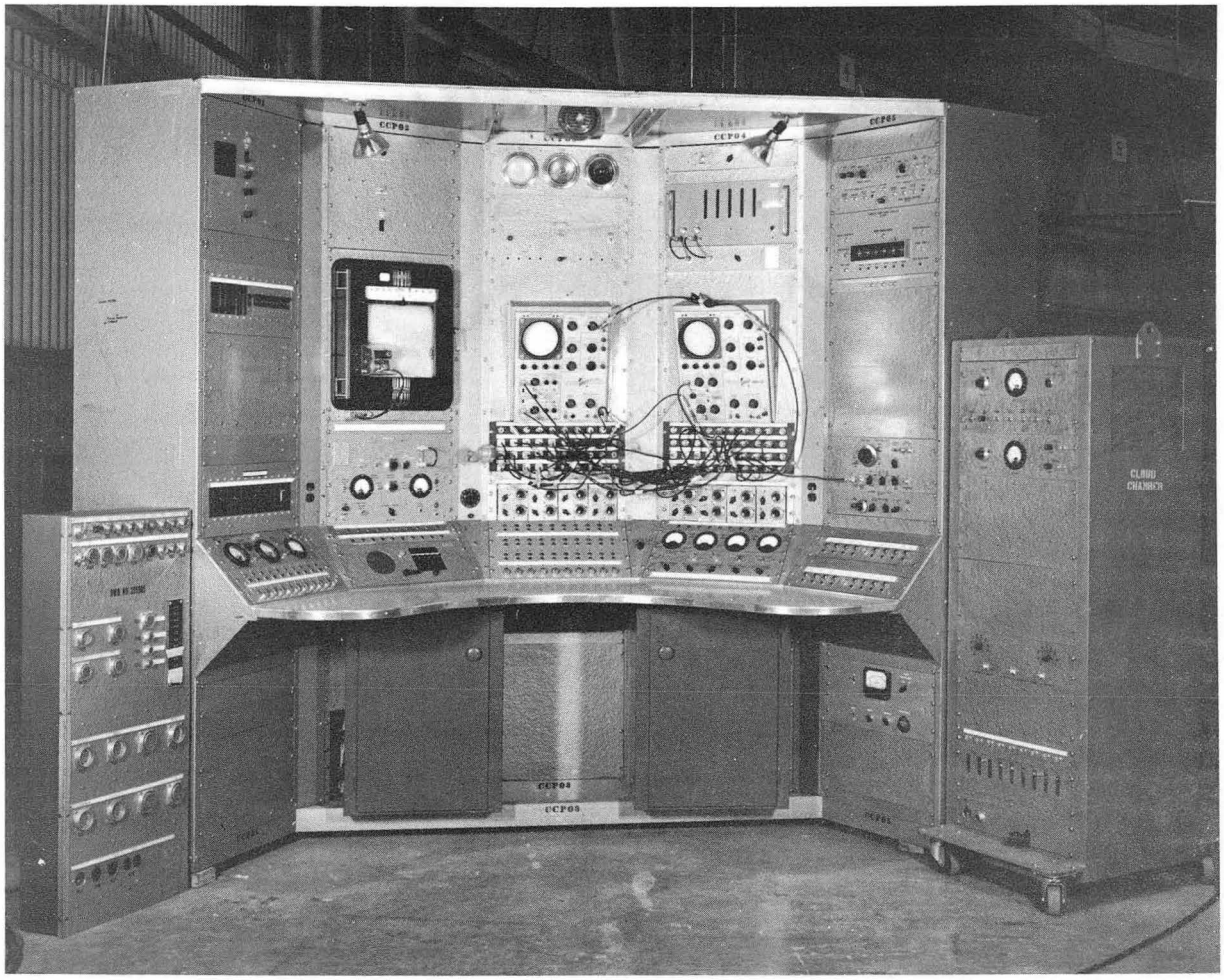

ZN-2260

Fig. 4. Photograph of the console.

Pion Beam

Trajectories followed by 5.5 Bev/c mesons were computed by Howard White using the IBM 650. The chamber then was set so that negative pions of this momentum passed down its center. The operation of the quadrupoles resulted in an image of the target at the chamber 2.8-in. wide by 1-in. high. The momentum spread was about 80 Mev/c per inch. The uncertainty in momentum at any point in the chamber was thus 224 Mev/c.

In Fig. 5 we have plotted the measured momentum distribution of 144 beam pions that scattered elastically off of hydrogen. The momentum of a track was measured by the use of a digitized microscope. The methods employed in the measurement of momenta and angles are discussed presently. The mean momentum, as measured by the microscope, is 5.14 ± 0.43 Bev/c. Figure 5 also contains a dotted histogram that represents the momentum distribution of the incoming tracks of events constrained to be elastic. The constraints technique is described in more detail in a later section. The mean momentum, calculated from the dotted histogram, is 5.17 ± 0.27 Bev/c. The quoted errors are standard deviations.

The histograms in Fig. 5 exhibit a rather wide spread, although that of the dotted one is noticeably less than the other. This spread reflects the inherent difficulties of measurement at this high energy.

The variation in beam momentum across the chamber, calculated from wire orbits, is shown in Fig. 6. It is seen that there was a linear decrease from left to right. The curve is taken from data obtained by Birge[15] using wire orbits to determine the momentum distribution.[15] The distribution in Fig. 6 was combined with the observed flux distribution of Fig. 7 in the calculation of the mean beam momentum. A value of 5.32 ± 0.08 Bev/c was obtained. When we combine the three calculations of the mean momentum, we obtain 5.21 ± 0.04 as the grand mean. In our calculations of cross sections the value 5.17 ± 0.05 was used. This

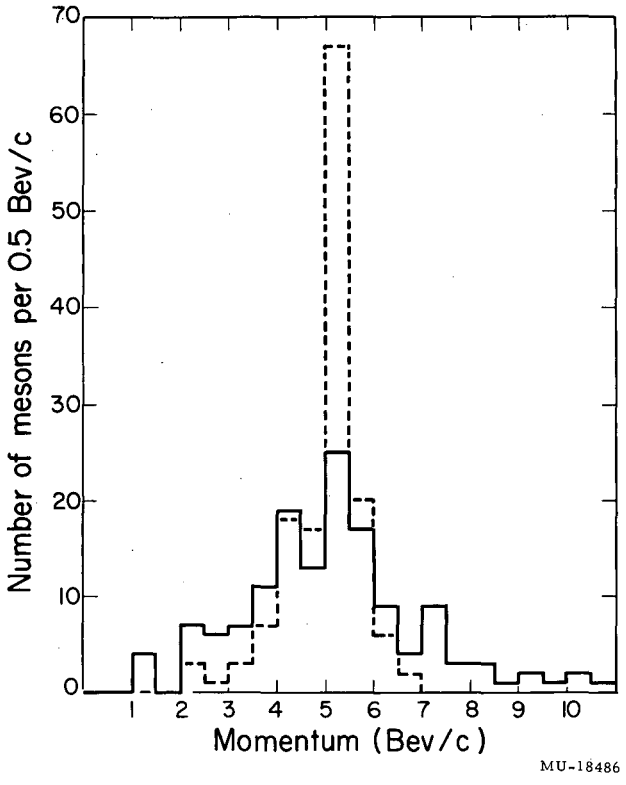

Fig. 5. Momentum distribution of 144 elastic events. The dotted histogram was obtained by the method of approximate linear constraints.

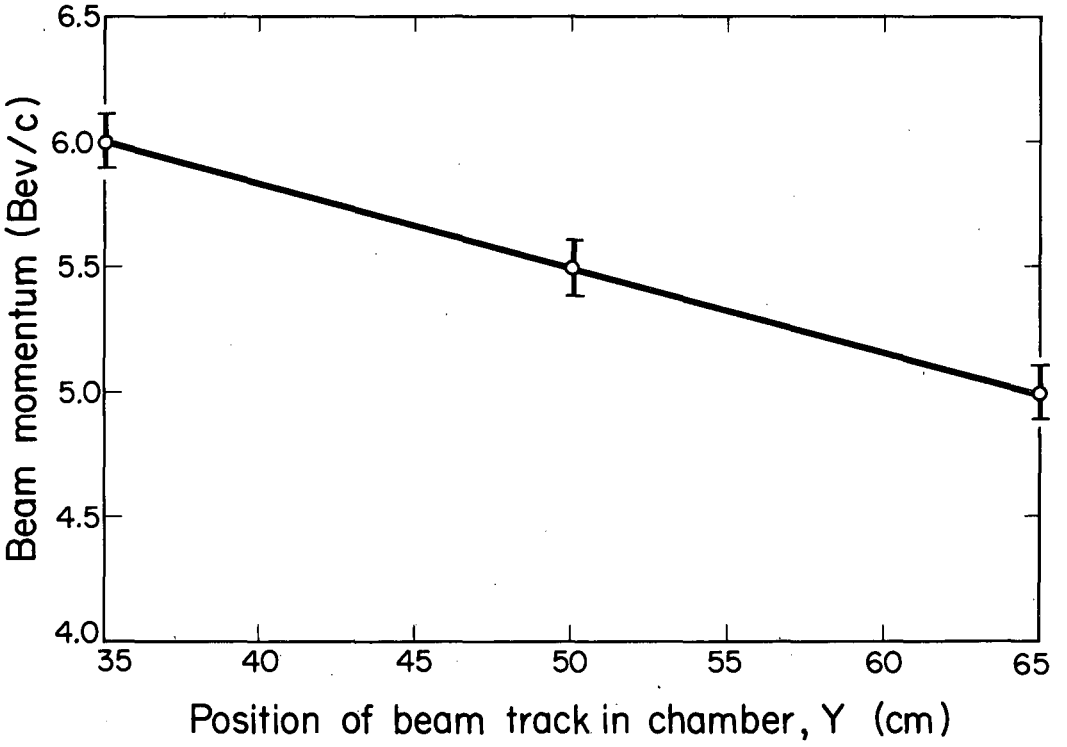

Fig. 6. Variation of beam momentum across the chamber. Taken from data obtained by R. Birge[15] using 1-in. by 1-in. counters. The position of the center of the chamber is 50 cm.

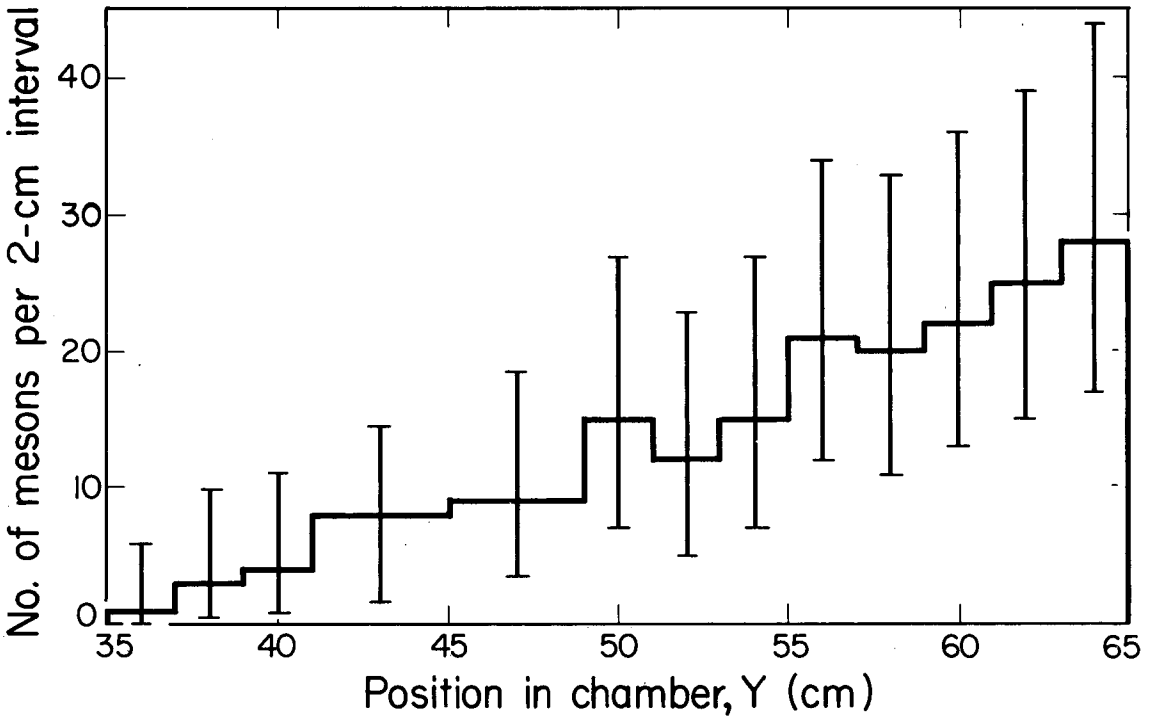

Fig. 7. Meson flux distribution across the chamber. The position of the center of the chamber is 50 cm.

value and the error are the result of a qualitative appraisal of the three methods and the relative merits of each. In view of the closeness of the three values of the mean momentum and the grand mean, it was felt that the relatively large errors above associated with two of the values represent measurement errors of beam tracks. It is also believed that the higher average of 5.32 Bev/c results from a fairly large fraction of the beam that underwent single and multiple scattering in the air and walls of the chamber. Such scattering could cause particles originally on the low end of the momentum curve to enter the region of high momentum.

The result of the small (1-in.) vertical image of the target at the chamber was the concentration of the mesons in a height of only 3 centimeters (cm). In Fig. 8 one sees that 75.6% of the beam was in the region of this height. The observed distribution is seen to be in accord with that obtained by Birge, which is represented by the solid curve. From Fig. 8 an average height of 59.06 ± 0.55 cm was computed. The beam was thus centered 0.81 cm above the median plane of the chamber.

Scanning

Each picture bears a number, and corresponding views were scanned simultaneously for two-prong Formica event of interest. Scanning was done on a machine that has two projectors mounted above a horizontal sheet of Formica that serves as the screen. Each view can be seen separately or the two can be superimposed. A roll of film containing 250 pictures was finished before another roll was begun.

Approximately 53,000 pairs of pictures were taken during the run. Many of the photographs were unacceptable. Some of the more commonly encountered reasons for rejection of a particular picture were:

(a) Beam flux too high

(b) The existence of a large bubble over a considerable portion of the chamber, indicative of insufficient pressure and (or) incorrect timing

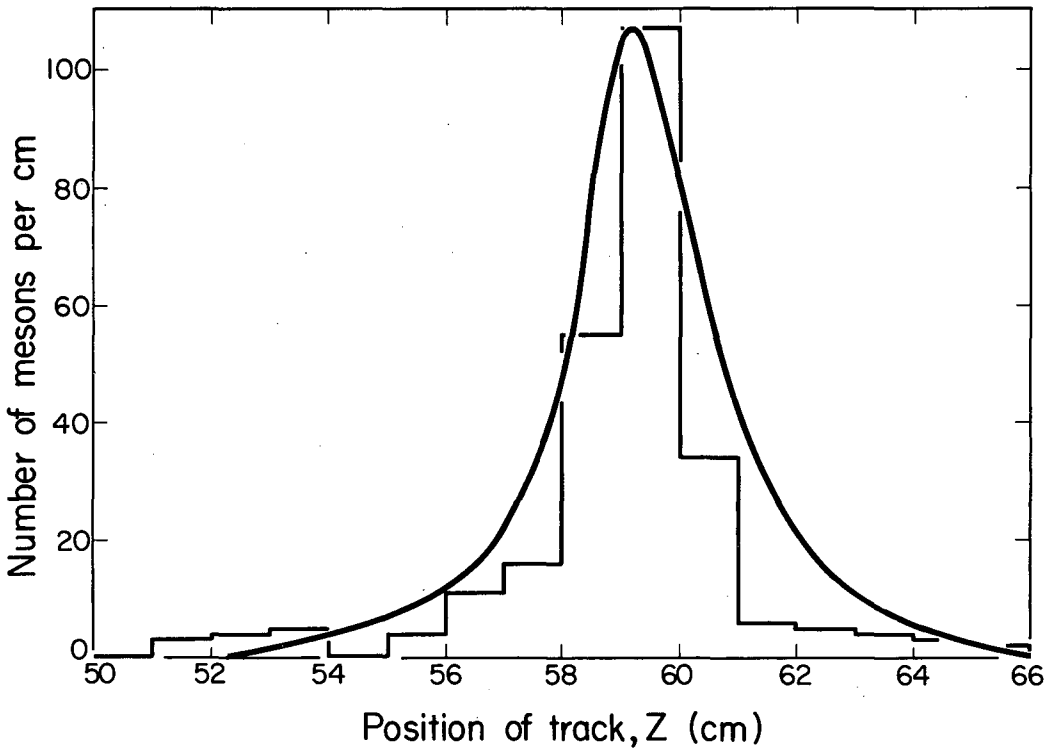

Fig. 8. Height of beam tracks in the chamber. The position of the bottom glass is 50 cm. The solid curve is taken from observations by R. Birge[15] using 1-in. by 1-in. counters.

(c) Poor and insufficient illumination of the tracks caused by failure of some of the lights

(d) Failure of one of the cameras to wind after an exposure resulting in double exposure

(e) One view missing.

The changes in operating conditions responsible for each of the above defects occurred occasionally throughout the run, but irregularity in beam flux occurred most frequently. Because of this, we used a smaller region of the chamber and restricted the number of beam tracks per picture to a smaller value in those pictures that were used for flux counting than we did for accepting events generally. The two regions, called A and B, respectively, are seen in the outline of the bottom glass of the chamber, Fig. 9. Region A is 40 by 30 cm; B, 50 by 40 cm. Both extend the depth of the chamber, i.e., 6-1/2-in., and are well-defined by lattices of white dots painted on the top and bottom glasses.

Acceptance Criteria for Events and Pictures

The following requirements were imposed on all two-prong events and pictures:

(a) Since the number of beam tracks and their curvature in a particular region are not the same in each view, we required, first of all, that when it was necessary to make a distinction between the views, view 1 be chosen.

(b) The projected origins of those events for which the number of tracks and pictures were counted were restricted to lie in region A, while the larger region, B (which encloses A), contained the projected origins of all events.

(c) The azimuthal angle, β (Fig. 10), that each beam track made with the x axis at one of the upper boundaries was required to lie in the interval $3\text{deg} > \beta > -3\text{deg}$. The distribution of β is shown in Fig. 11. The center appears considerably displaced relative to the x axis because all

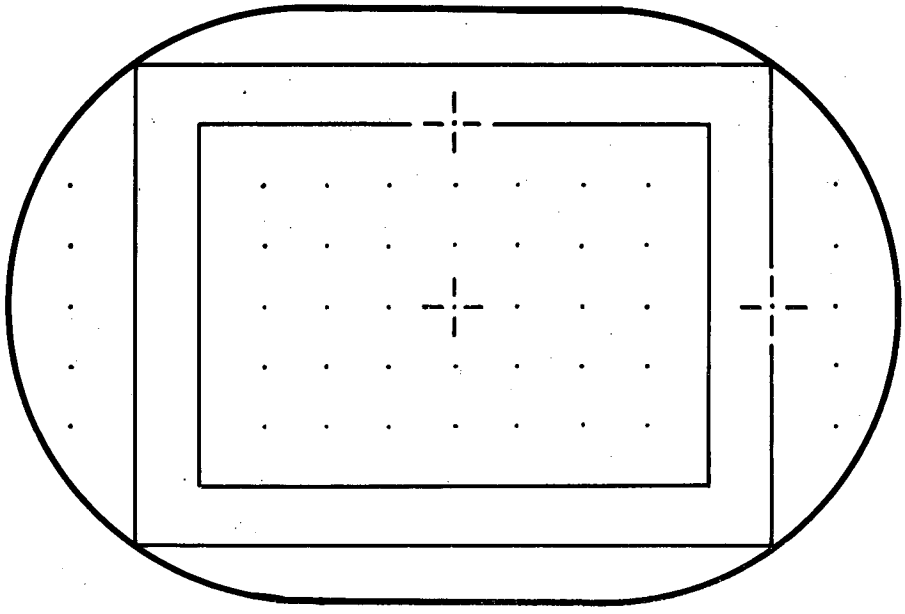

MU-18490

Fig. 9. Outline of bottom glass of chamber. Region A is bounded by inner rectangle; B, by outer rectangle. The horizontal or vertical distance between two adjacent dots is 5 cm.

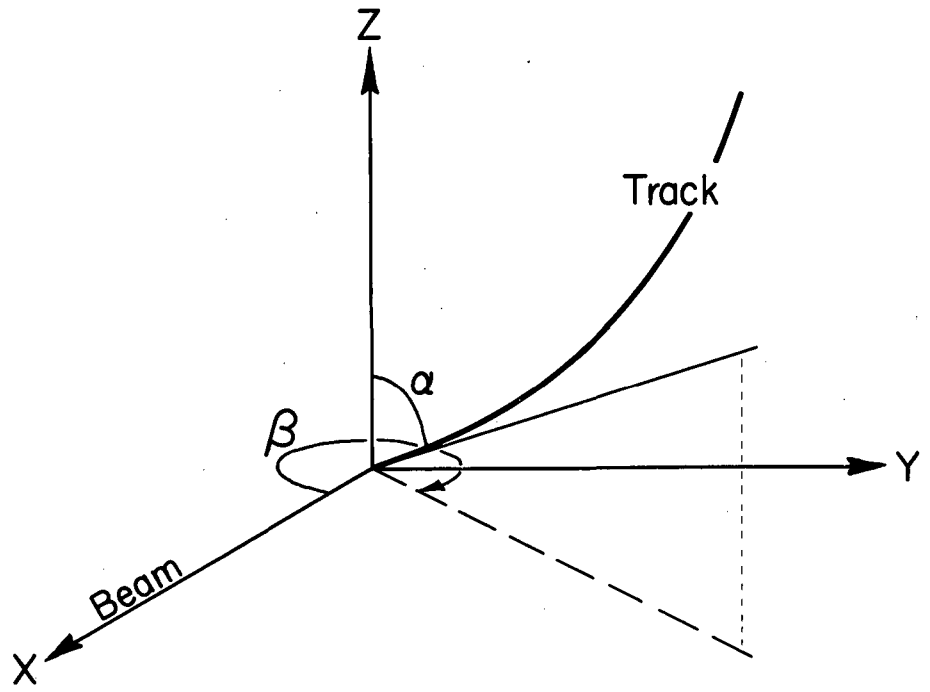

Fig. 10. Spatial coordinates used in measurements on tracks.

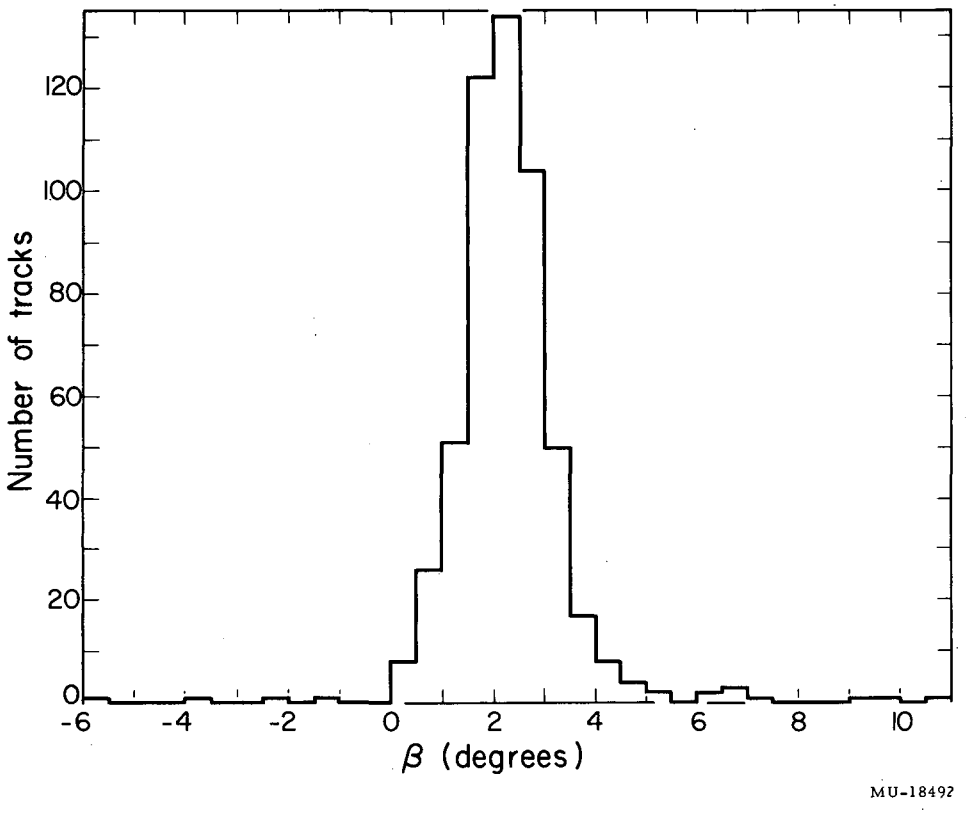

Fig. 11. Distribution in β of beam tracks $\geq$ 30 cm.

of the tracks in the sample were $\geq$ 30 cm long and were measured at the point of interaction of the event. One calculates that a track of 35 cm is turned through $\sim$1.8 deg in a 13.5 kilogauss field. The center probably lies between 0 and 1 deg at the upper boundary. The mean of the distribution was found to be 2.3 deg while the standard error is 1.2 deg. The criterion corresponds to a spread of $\sim$2.5 standard deviations

(d) The dip angle, α, that each beam track made with the vertical was required to be 89.5 $\pm$ 3.5 deg. The distribution in α is plotted in Fig. 12 for 506 beam tracks having $|\beta| \leq 3$ deg. The average is 89.5 deg, and the error in the distribution, σ = 2.7 deg.

(e) For a picture that was used in the flux counting, the number of beam tracks that entered region A was restricted to twelve or less;

(f) Radii of curvature of incoming tracks as measured by ruled templates had to correspond to mean beam curvature.

(g) The origin of an event had to be clear in both views.

(h) Beam tracks were further defined to be those that either traversed the entire region or remained wholly in the region until they interacted. From Fig. 8 it is seen that only two of the two-prong events have origins that lie within 1 cm of either glass. It is therefore reasonable to assume that a track that leaves the top or bottom glass of the chamber before traversing the region and before interacting is not a beam track. Because of the small number of beam tracks in the vicinity of the glasses, the number rejected by this criterion is considered negligible.

(i) All beam tracks are consistent with minimum ionization. The restrictions on the number of beam tracks in a picture, and the confinement of some projected origins to region A, were imposed to facilitate flux counting. In those pictures that were not used for this purpose, no sharp limit was placed on the number of beam tracks. A picture that was scanned under this condition, however, was required to have a number and distribution of tracks such that no bias would likely result in accepting two-prong events therefrom.

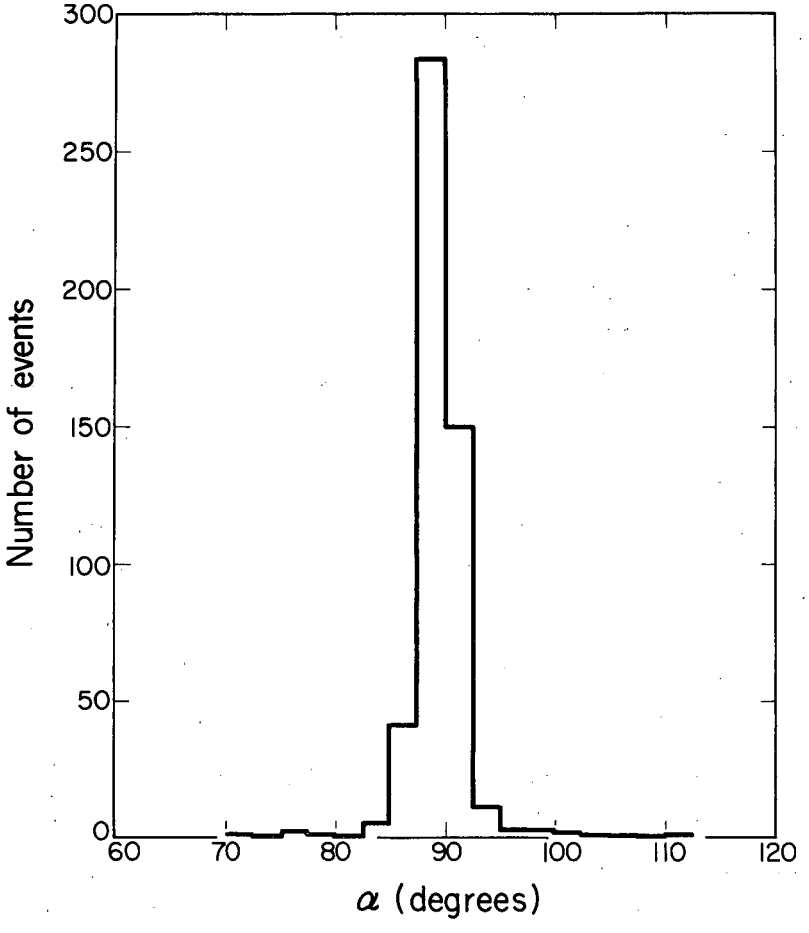

Fig. 12. Distribution in α of beam tracks ≥ 30 cm and with $|\beta| \leq 3^{o}$.

Approximately 11,000 pictures were scanned. When a two-prong event was found, it was sketched on an especially designed keysort card that contains an outline of the bottom glass of the chamber. The event was sketched in the same position, relative to the fiducials, that it occupies on the film. This procedure facilitated the location of the event under the microscope. In addition, the picture number, number of outgoing prongs, and number of beam tracks were recorded in appropriate places on the card. Adjacent to the sketched track there was a number that was later used to identify it. We used 0 for the incident track, 1 for the scattered meson, and 2 for the recoil proton. Because a more reliable determination of the nature of a two-prong event can be made when the proton stops than when it leaves the chamber each proton track that did not leave the sides was investigated to determine whether it stopped in the liquid. For those that did stop, an indication of this fact was also placed on the card. This procedure guaranteed that the full length of the track would be measured.

At every tenth picture the number of beam tracks and the positions of all events relative to the fiducials were recorded on separate sheets of paper. Also recorded were picture numbers of all nonusable pictures on a roll. This information was used in the determination of the path length.

MEASUREMENT

The method of measurement is similar to one previously described and will be discussed here only briefly.[16] A digitized microscope is used to obtain coordinates of points along a track relative to the fiducials in each of the two views. These points are punched on IBM cards. A set of rectangular coordinates is chosen with x lying parallel to the long dimension of the chamber (Fig. 10). The spatial coordinates corresponding to the points previously obtained are next determined.[17] These coordinates now define the trajectory followed by the particle. The azimuthal angle β is determined from the projection of the helix on the xy plane. The xy projection is also used in the calculation of the radius of curvature, ρ. The dip angle, α, is obtained from the projection of the helix on the xz plane. The momentum of the particle is calculated from the known values of the magnetic field and the radius of curvature.

The computation of momenta and spatial angles of tracks and their associated errors is performed on the IBM 650. The output giving these quantities is called Fog III. Other programs, to be discussed presently, were used to test the kinematical relations that characterize an elastic event.

The meson scattering angle, θ_m, and the proton scattering angle, θ_p, can be calculated from the space angles α and β by use of the formula

$$\cos \theta_j = \cos \alpha_0 \cos \alpha_j + \sin \alpha_0 \sin \alpha_j \cos (\beta_j - \beta_0) \qquad (1)$$

for $j = m, p$. The subscript 0 refers to the incident meson. The meson scattering angle is sufficiently small at this energy to justify the use of the approximate formula

$$\theta_m^2 = (\alpha_m - \alpha_0)^2 + (\beta_m - \beta_0)^2 . \qquad (2)$$

Equation (2) was used to calculate this angle in most cases.

As a measure of the coplanarity of an event, the angle ψ that track 1 (the scattered meson) makes with the plane formed by tracks 0 and 2 was calculated. The three angles, θ_m, θ_p, and ψ are determined in Program 39.

A more powerful technique that utilizes all of the equations that the parameters of an elastic event satisfy is embodied in Program 49. The method is that of approximate linear Lagrangian constraints and has been described.[18] Using this procedure, one calculates the most probable values for the nine variables involved in a two-prong event, assuming it to be elastic, and compares these with the measured values. The constraining equations are

$$F_1 = p_1 \cos \theta_1 + p_2 \cos \theta_2 - p_0 , \tag{3}$$

$$F_2 = p_1 \sin \theta_1 - p_2 \sin \theta_2 , \tag{4}$$

$$F_3 = \begin{vmatrix} \lambda_0 & \mu_0 & \nu_0 \\ \lambda_1 & \mu_1 & \nu_1 \\ \lambda_2 & \mu_2 & \nu_2 \end{vmatrix} , \tag{5}$$

and

$$F_4 = E_1 + E_2 - E_0 - M_H . \tag{6}$$

In Eqs. (3) and (4) the p's represent momenta. It can be seen that these equations express the momentum unbalance along, and transverse to, the direction of the incident particle. In Eq. (5), which expresses the noncoplanarity of a two-prong event, we have

$$\lambda_j = \sin \alpha_j \cos \beta_j ,$$
$$\mu_j = \sin \alpha_j \sin \beta_j ,$$

and

$$\nu_j = \cos \alpha_j ,$$

for $j = 0, 1$, and 2. In Eq. (6) the E's represent the energies of the particles, while M_H is the proton rest mass, 938 Mev. This equation expresses the energy unbalance in the interaction. Introducing the Lagrangian multipliers, a_λ, one finds the most probable values by minimizing

$$M(\chi_i a_\lambda) = \sum_{i=1}^{9} (\chi_i - \chi_i^m)^2/u_i + 2 \sum_{\lambda=1}^{4} a_\lambda F_\lambda(\chi_i) . \quad (7)$$

The quantities χ_i^m are the measured values of the variables, and the u_i are the variances.

Because of the nonlinearity of the constraining equations, the process of minimizing Eq. (7) is actually an iterative one.

IV. IDENTIFICATION OF EVENTS

Most elastic events at this energy possess certain visual characteristics that permit their tentative identification in the process of scanning. Since this is primarily small-angle scattering, a considerable fraction of the elastic events is expected to have recoil protons that stop in the chamber; we found that 63% of the elastic events have stopping protons. The tracks made by these particles have an ionization that is well above minimum. The scattering angle of the proton is in the neighborhood of 60 to 85 deg in general. The track of the scattered meson shows minimum ionization and makes a small angle of the order of 2 to 5 deg with the beam pion. These angles were measured roughly with a protractor in the process of scanning, and good agreement with computed values resulted when the scattering plane was fairly flat.

With the aid of the programs outlined previously, more definite conclusions were reached as to the identity of the nearly 2000 events submitted for measurement after the following kinematical conditions were imposed that all elastic events must satisfy:

(a) Angular correlation. The incident pion momentum was assigned from the wire-orbit calculations according to the location of the origin of the event in the chamber, and tables containing the correlated angles as a function of incident momentum were used. The fact that this procedure may have resulted in an overestimate of this momentum gave a negligible error.

(b) Momentum and energy conservation. These requirements could not be imposed because momentum measurements were not sufficiently accurate to be meaningful.

(c) Correlation of proton range and proton scattering angle for stopping recoils. This requirement is related to (a) and was imposed in the 63% of the cases in which the proton stopped in the liquid. It is the most reliable criterion, since the range can be determined with a higher degree of precision, in general, than any of the other parameters.

(d) Coplanarity. The coplanarity angle ψ is zero within experimental error for an elastic event.

With the measured angles, we again looked at the events on the projector. This procedure aided in the identification of the events and prevented the accidental loss of elastic scatters due to gross errors of measurement. The measured scattering angles were plotted as points on graphs of θ_p vs. θ_m as a function of incident momentum. Figure 13 shows a set of the curves that were used, and in Figs. 14 and 15 is plotted the angular correlation of a sample of the elastic events for which the meson scattering angles are ≤ 9 deg. The identity of these events was firmly established after a study of errors, which are considered presently. At this stage of the analysis the results from the plot were compared with those from Program 49.

In principle, classification of an event can be made unambiguously from the results of this program. The output contains the magnitude and sign of the quantities F_1, F_2, F_3, F_4, and M. In addition, this program gives the changes in the nine variables and their final most probable values, if we assume an elastic event. The F values for elastic events range from $\sim |10^{-3}|$ to $|10^{-8}|$, while for inelastic events the range is from $\sim |10^{-1}|$ to $|10^{-4}|$. We deduced that a value as large as 50 for M was not unreasonable for an elastic event of poor measurability, and in a few cases even larger values were admitted. We also found that, while inelastic events generally have M values greater than 50, a rather large fraction ($\sim$ 20%) have values of 50 or less. The M value distribution

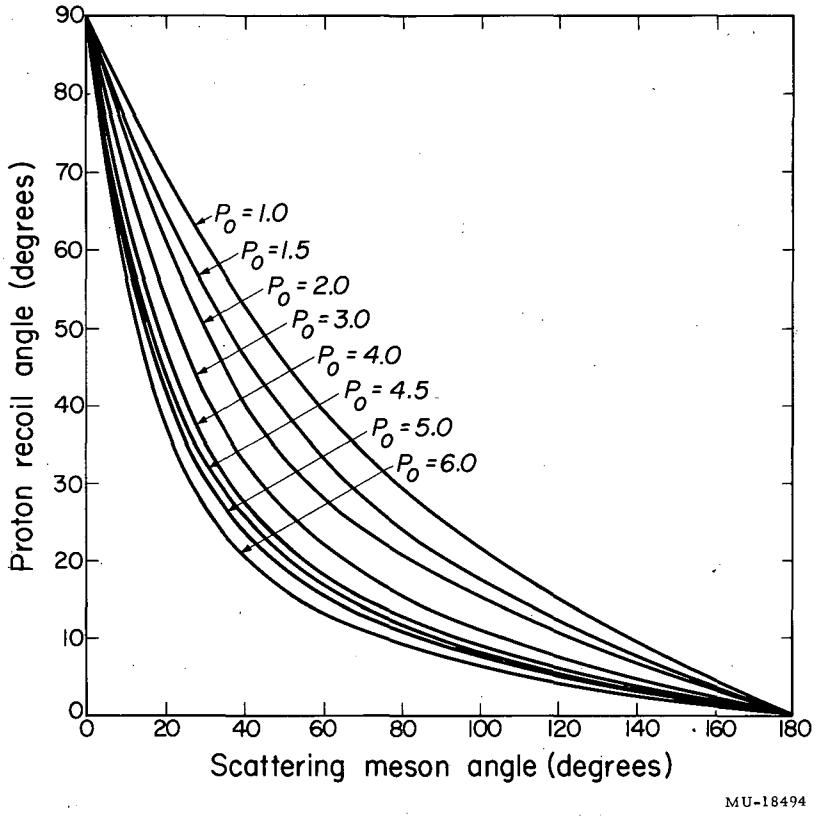

Fig. 13. Proton recoil angle vs scattered meson angle (laboratory system) for elastic π-P collisions for various P_o in Bev/c.

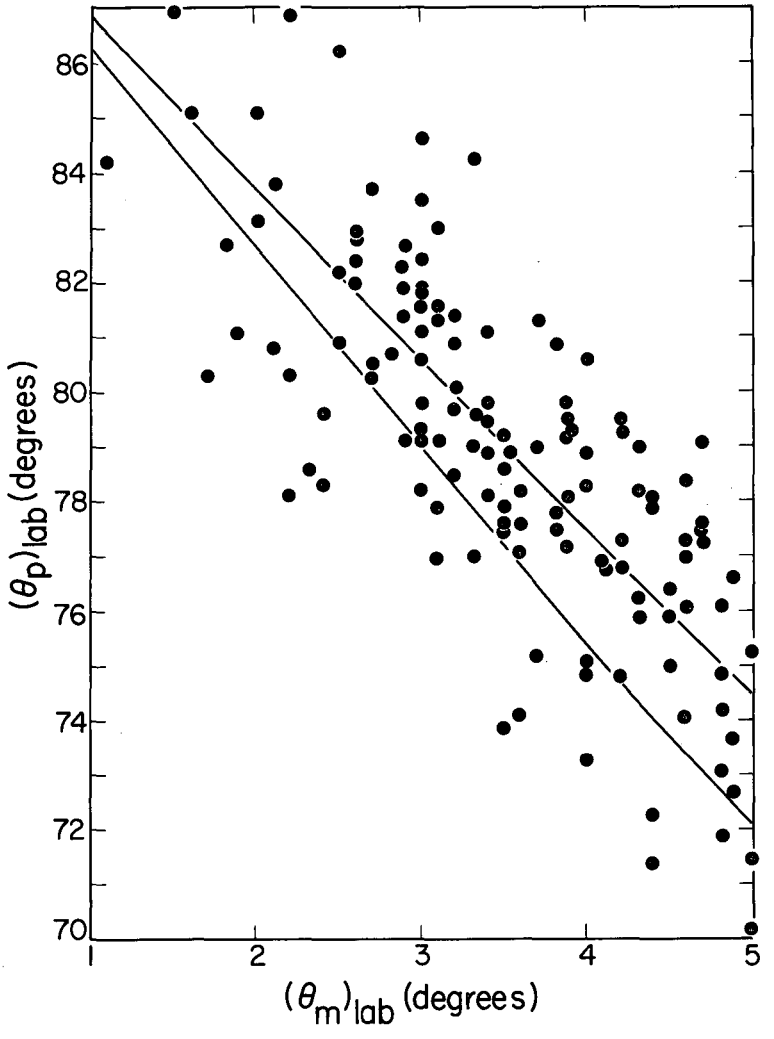

MU-18495

Fig. 14. Angular correlation of elastic π-P events. The solid curves show the correlated scattering angles for incident pion momenta of 5 Bev/c and 6 Bev/c, respectively.

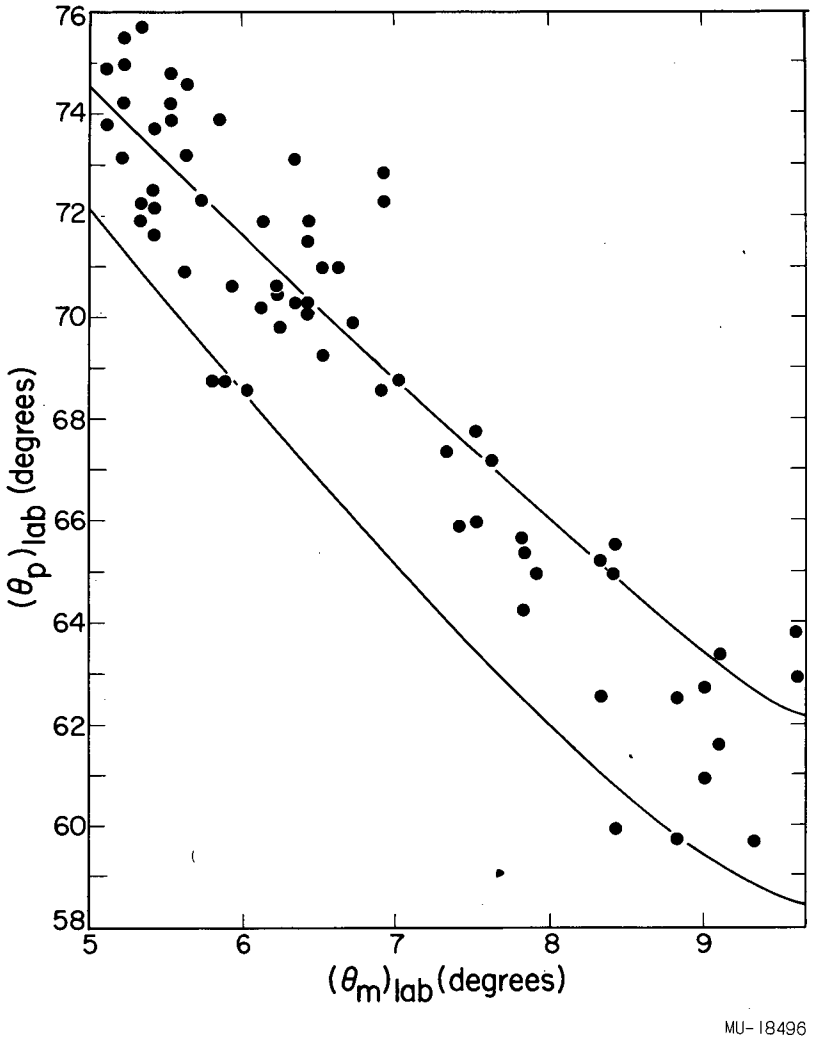

Fig. 15. Angular correlation of elastic π-P events. The solid curves show the correlated scattering angles for incident pion momenta of 5 Bev/c and 6 Bev/c, respectively.

for the elastic events is shown in Fig. 16. The tail of the distribution is due to elastic events having poor quality, and to background events indistinguishable from the elastics.

Comparing the results from the two methods, we found that they were in agreement most of the time. In 15% of the cases, however, the conclusions drawn from the two as to the identity of an event were not in agreement. It was found that the assumed errors used in Program 49 were incorrectly estimated in those cases where there was disagreement, and the final decision was made following a more searching study of the errors.

V. DISCUSSION OF ERRORS

Of the two-prong events, those having $\theta_p \geq 90^\circ$ were classed immediately as inelastic. Those in which both tracks were on the same side of the incoming beam also were classed as inelastic. This left 811 of the $\sim$2000 two-prong events seen. Half of the events retained had protons that came to rest in the liquid. Particular attention was paid to these events because the momentum of the proton in each could be accurately determined from the range.

If angle and momentum measurements had been made with very great accuracy, the background from carbon events would have been negligible. Since this was not the case, it became essential to make an accurate determination of the errors and to check them empirically wherever possible. Three sources of error are (a) optical distortions in the oil above the chamber due to nonuniform temperature of the oil, (b) resetting difficulties made during measurements on the microscope both on clear and distorted tracks, and (c) multiple scattering affecting curvature measurements and measurements of angles.

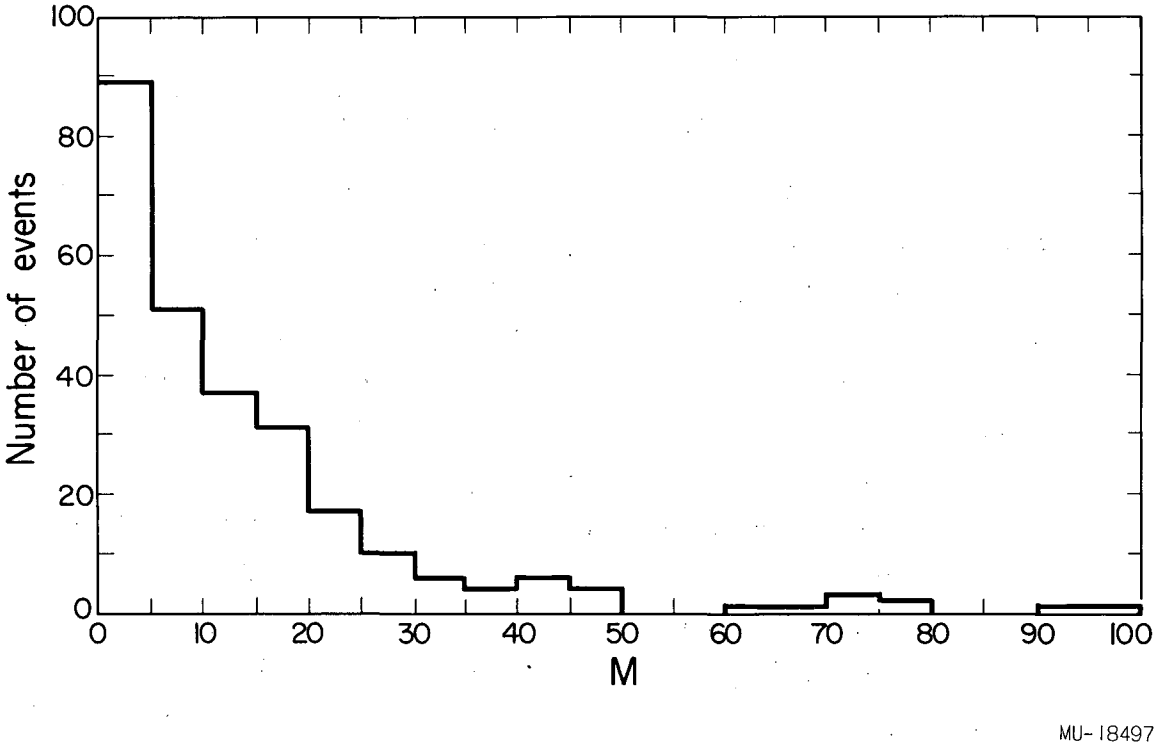

Fig. 16. Distribution in M for elastic events.

Momentum Errors

A study of (a) and (b) was made by repeatedly measuring nine beam tracks. The results of this study are presented in Table I. The average length of each track measured appears in column 2, while column 3 contains the average measured momentum. Column 4 shows the average sagitta, and the next column the average error due to resetting. In column 5, S_i refers to the individual measurements. The error in the average sagitta due to oil distortions appears in column 6. The true value of the sagitta S_t, was calculated on the basis of the wire-orbit determination of momentum. The over-all average error in sagittae due to distortions is seen to be 0.026 cm, and that in resetting is 0.007 cm. If we eliminate the two worst cases, which were chosen because of exceptionally large distortions, the average sagittal error drops to 0.016 cm and the error in resetting to 0.0054 cm. These two quantities are most suitable for 80% of the pictures. They determine errors in curvature measurements and angles when multiple scattering is negligible.

Angle Errors

The stereoscopic angle of the lenses magnifies vertical errors by a factor of six, making these errors due to oil distortion ±1 mm. The distortions cover some 5 cm of track and therefore do not cause appreciable errors in the angles of a track considerably shorter than this. A flat track 0.8 cm long would have a resetting error of 0.005 cm multiplied by $6\times \sqrt{2}$ giving a vertical tilt of 0.042/0.8 radians, or 3 deg. This error decreases inversely with the length of the track, except for the effect of oil distortions, and beyond a certain length one expects it to be negligible. This behavior was verified by a study of the errors in the proton scattering angles of 75 elastic events in which all of the protons stopped in the liquid (Fig. 17). The scattering-angle errors are defined by

Table I

Results of repeated measurements on nine beam tracks

Picture	$\overline{L}$ (cm)	$\overline{P}_0$ (Bev/c)	$\overline{S}$ (cm)	$\lvert\overline{S-S_i}\rvert$ (cm)	$\lvert\overline{S}-S_t\rvert$ (cm)	Measures
238311	18.2	2.29	0.073	0.017	0.045	10
238761	52.80	5.30	0.266	0.003	0.016	5
239041	6.50	1.33	0.016	0.014	0.012	10
23968	47.9	6.01	0.193	0.004	0.026	7
31028	38.0	3.84	0.190	0.011	0.059	10
33025	18.69	4.30	0.041	0.007	0.007	9
35312	34.52	4.82	0.125	0.005	0.016	8
39561	48.71	5.85	0.205	0.004	0.023	9
53852	13.09	2.98	0.029	0.001	0.012	8

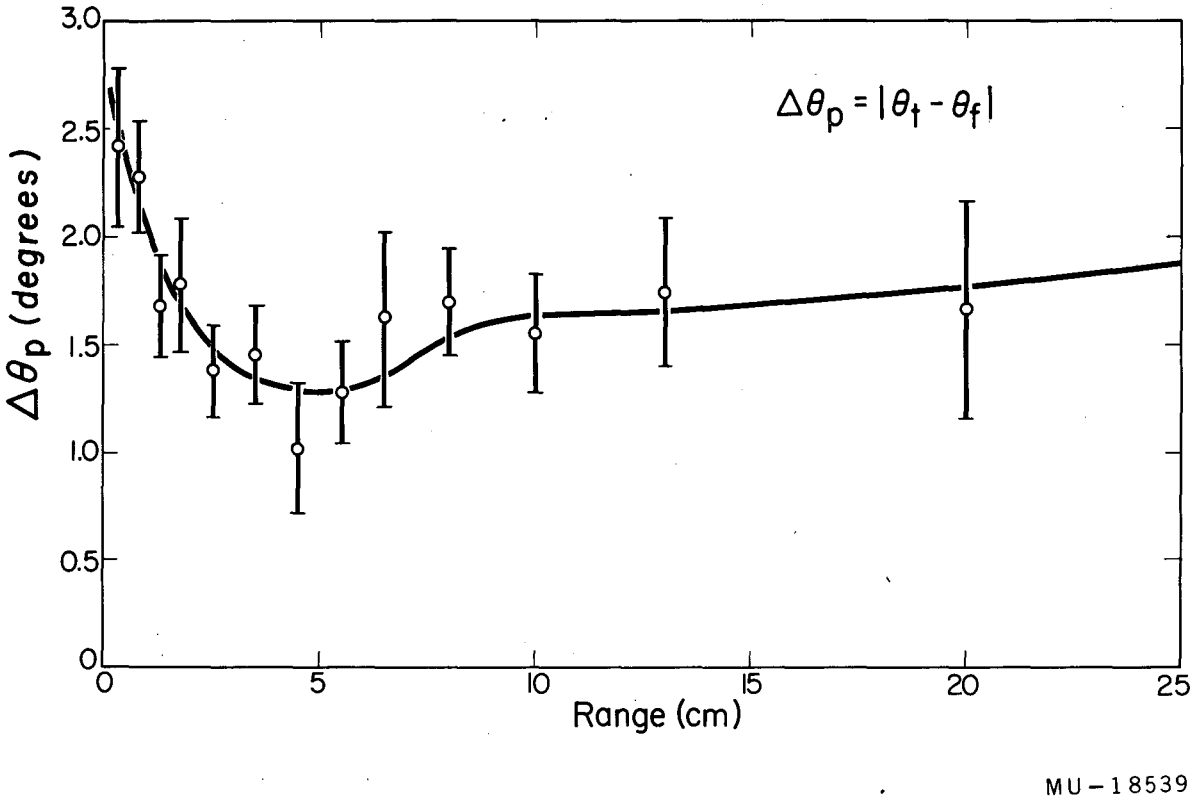

Fig. 17. Proton-scattering-angle errors of elastic events as a function of range.

$$\Delta\theta = \left| \theta_t - \theta_f \right| , \qquad (8)$$

where θ_t is the tabulated scattering angle for an elastic event with incoming momentum equal to the wire-orbit value and a proton range equal to the measured value. The angle θ_f is that computed from data contained in Fog III and given in Program 39. The graph shows a noticeable rise for protons with ranges $R \leq 1.5$ cm.

Multiple scattering produces a negligible error in the angles of the high-momentum mesons that we are considering here, but causes errors in the proton momenta and scattering angles. The effect on the scattering angle of the proton is seen in Fig. 17. The rise in the curve for $R \geq 5$ cm is presumably due to multiple scattering.

VI. CORRECTIONS TO THE OBSERVED DATA

Scanning Efficiency

Corrections for events missed in scanning were made in the following way. All film was scanned twice giving N_1 and N_2 events. If N is the true number of events in the film, then $e_1 = N_1/N$ and $e_2 = N_2/N$ are the respective scanning efficiencies. The number of events N_{12} found by both are assumed to be $N_{12} = e_1 e_2 N$. On this basis e_1 is $80 \pm 5\%$, e_2 is $87 \pm 3\%$, and the efficiency for the double scan is $1 - (1-e_1)(1-e_2) = 98 \pm 1\%$. The number of elastic events must be multiplied by the factor $C_s = 1/0.98 = 1.02 \pm 0.01$.

Background Events

Since the cross section for inelastic processes of the type

$$\pi^- + p \rightarrow \pi^- + p + n\pi^0$$

for $n = 1, 2, 3$, etc. rises with energy, one expects to find more events of the above type at 5 Bev than at lower energies. These processes occur both with the free protons of hydrogen and the semifree protons of carbon. The problem of separating these inelastics from the true elastics is made particularly difficult because the characteristic length for pair production is rather long ($\sim$ 109 cm) in propane. Therefore, one does not expect to see many of the pairs in this chamber. Indeed, one of the scanners recorded only 49 out of the 2000 events that had one or two visible pairs, and while no systematic attempt was made to note the frequency of occurrence of such events, this figure may be taken as an indication of the number present. The true number in the film scanned probably does not differ from 49 by more than a factor of two. The quasi-elastic process $\pi^- + p \rightarrow \pi^- + p$ that involves one of the protons of carbon also contributes to the background. The correction factor that was applied to the elastic events to account for background was estimated from the following considerations.

In determining which events occur in hydrogen it is important to make the region of acceptance wide enough to include the greater part of the elastic scatters, and, at the same time, narrow enough to exclude, as far as possible, inelastic events.

The angle θ_m of the scattered meson had an average error derivable from the repeated measurements of sagittae where the error was found to be 0.026 cm. If we assume that the same error is made independently at the two ends of a long track, this amounts to $0.026 \times \sqrt{2}$ or 0.037 cm horizontal displacement of one end of a track with respect to the other. This results in a vertical error of 6×0.037 cm or 0.22 cm since the distortions often show in only one view. In a 15-cm track this produces an error in the dip angle, α, of 0.84 deg. Some small scattering takes place which is not found in scanning. It was considered reasonable to multiply this error by 3 to assure that most elastic events were kept. The maximum error, $\Delta\theta_m$, in the meson scatter angle was taken to be 2.5 deg.

The coplanarity angle, ψ, is defined as the angle between the scattered pion and a plane defined by the incoming pion and the proton. Because of the way ψ is defined, it is obvious that for $\theta_m \leq 3.5$ deg the coplanarity angle cannot exceed 3.5 deg. The coplanarity distribution of the events that were tentatively identified as elastic by the angular-correlation plot (Fig. 14) showed a broad maximum for $\psi \leq 3.5^\circ$, and a very small tail beyond this angle. A value of 3.5 deg was taken as the limiting value of ψ for elastic events. For large values of θ_m, this coplanarity restraint begins to exclude inelastic events.

Elastically scattered protons for a 3-deg pion scatter have a range of $\sim$4 cm where already the proton angle is well determined with an average error of 1.3 deg. At larger meson scattering angles, the coplanarity requirement will exclude inelastic events, since the proton angle is determined with more than twice the accuracy required to satisfy this coplanarity constraint.

The errors in the proton angle $\Delta\theta_p$ have been discussed. They are greatest for short-range protons. As an additional check on these errors and also to find the background from inelastic events, a plot of the $\Delta\theta_p$ distribution was made for all events having stopping protons. The selected events were further required to have meson scattering errors and coplanarity angle errors consistent with the above requirements for elastic events. One expects the distribution to display some kind of gaussian-like character due to the elastic events, and a rather flat tail that represents background primarily. The histogram is reproduced in Fig. 18. It is seen to display these general features, though when we attempted to fit the distribution to a gaussian, a rather poor fit was obtained. In a study of the errors in the proton angle it was found that below ranges of 1 cm, the errors were considerably greater than for those above that range. Deleting the events with $R \leq 1$ cm from Fig. 18 gave the histogram in Fig. 19. The solid curve in the figure represents the gaussian fit to the data, if we assume a limiting error on the proton of 4.5 deg. The statistical error of the distribution of events within this range was calculated to be 1.92 deg. For a gaussian distribution, the corresponding average error is 1.5 deg. This value is seen to be in good agreement with the average error in Fig. 17. Under the assumption that the background is flat in the acceptance region, it was found that 10% of the accepted events are probably inelastic.

A similar plot was next made of the distribution of errors in meson-scattering angles. In this case the restrictions $\Delta\theta_p \leq 4.5^\circ, \psi \leq 3.5^\circ$ were applied to the selected events. The resulting histogram is shown in Fig. 20. Under the same assumption of a constant background, and a limiting error on the meson scattering angle of 2.5 deg, the background was found to be 3.5%. For the distribution of errors of 2.5 deg. or less, σ is 0.8 deg.

A plot of the distribution of coplanarity angles gave an even smaller background than the error distribution for the meson scattering angles. The largest effect, obtained from the $\Delta\theta_p$ plot, remains predominate and therefore fixes the background at 10%.

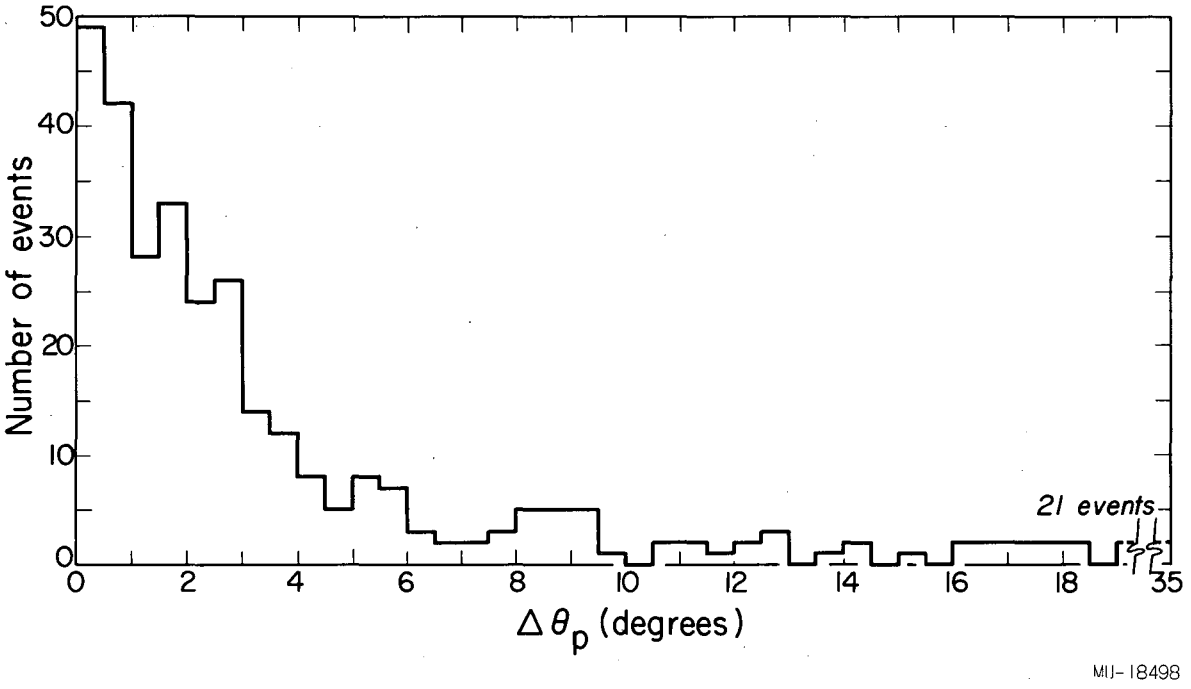

Fig. 18. Distribution of proton-scattering-angle errors for elastic and inelastic events having ranges and having $|\Delta\theta_m| \leq 2.5^o$, $\psi \leq 3.5^o$.

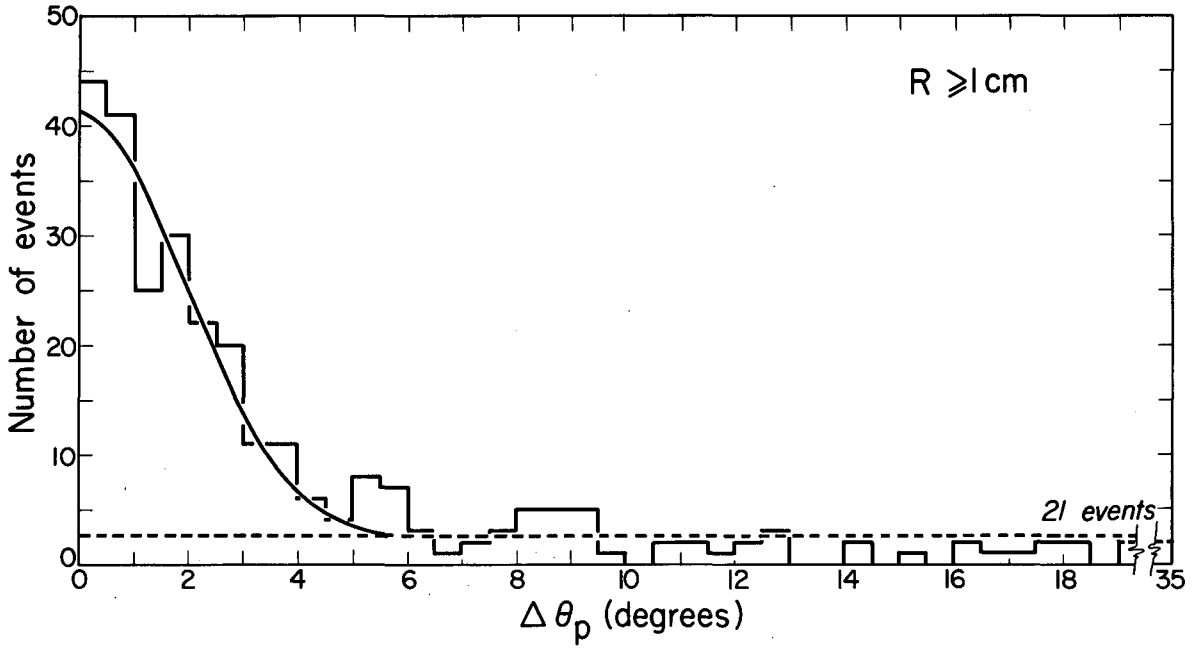

Fig. 19. Distribution of proton-scattering-angle errors for events having ranges > 1 cm and $|\Delta\theta_m| \leq 2.5^o$, $\Psi \leq 3.5^o$.

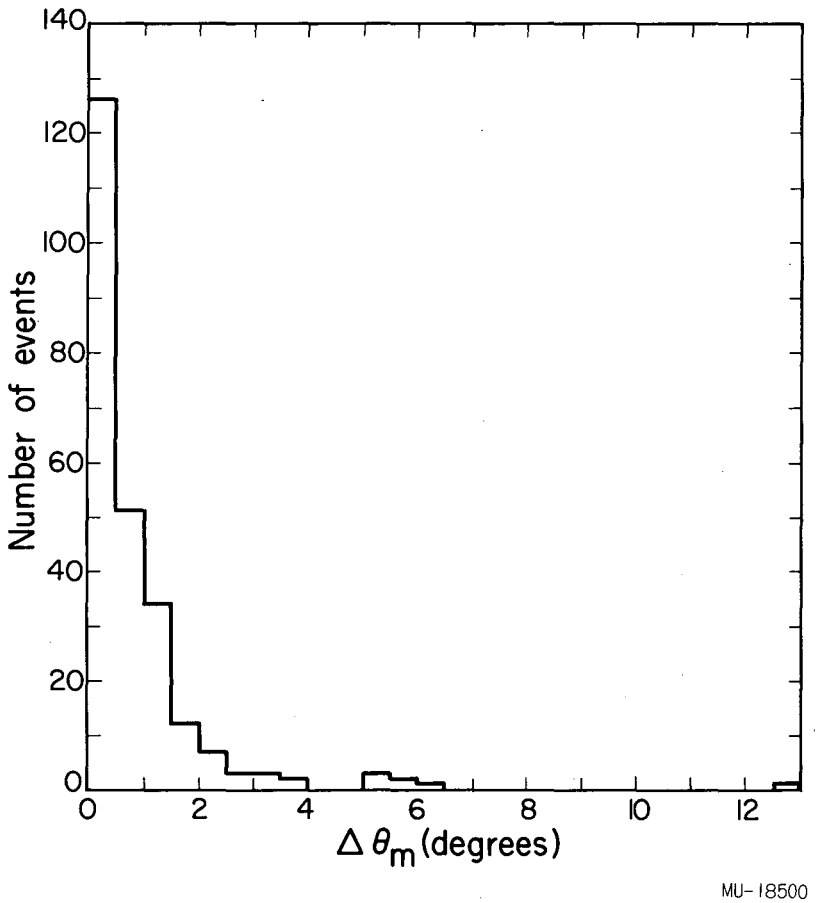

Fig. 20. Distribution of meson scattering angle errors for events having ranges and with $|\Delta\theta_p| \leq 4.5^o$, $\psi \leq 3.5^o$.

An attempt was made to see whether the quasi-elastic events peaked up under the elastic-scattering events. In order to do this, three plots were made of $\Delta\theta_m$, $\Delta\theta_p$, and ψ for inelastic events only. All events classified as elastic were excluded. The results are shown in Fig. 21. All of the events had stopping protons, and the same definitions of the errors apply. It is seen that the distributions in both $\Delta\theta_m$ and ψ tend to rise in their acceptance regions. This suggests the possibility that the meson scattering angles of background events are likely to be relatively small, and the coplanarity of these events is likely to be good by our criteria. The histogram in $\Delta\theta_p$ shows that the assumption of constant background is, in this case, a good one. Under the assumption that no strong correlations exist between the three angles for inelastic events, one can define probabilities P_m, P_p, and P_c that the errors in the meson scattering angle, proton scattering angle, and coplanarity of an inelastic event, respectively, will be less than the corresponding limits for elastic events. At least partial verification of this assumption was obtained by removing the inelastic events in the interval 3 deg $\leq \theta_m \leq$ 8 deg. We found that when these same events were removed from the $\Delta\theta_p$ histogram, the shape of the latter was left unchanged. With the large number of reactions that can take place at this energy, and the lack of a one-to-one correspondence between θ_p and θ_m in inelastic events, it is unlikely that strong correlations exist. From the three distributions one obtains $P_m = 0.428 \pm 0.03$, $P_p = 0.211 \pm 0.01$, and $P_c = 0.648 \pm 0.04$. The probability that an inelastic event simultaneously satisfies the three angular criteria (and is called elastic) is $P_m P_p P_c = 0.058 \pm 0.01$. The final separation of the events yielded 375 elastics and 436 inelastics. The background becomes $436/375 \times 0.058 \simeq 7 \pm (3)\%$. The error is larger than statistical, and reflects the uncertainty of the limits on the three angles. Using this figure, we must correct the number of elastic events by the factor $C_b = 0.93 \pm 0.03$.

The identity of the events that did not have stopping protons was made by assuming that the measured meson scattering angle was correct

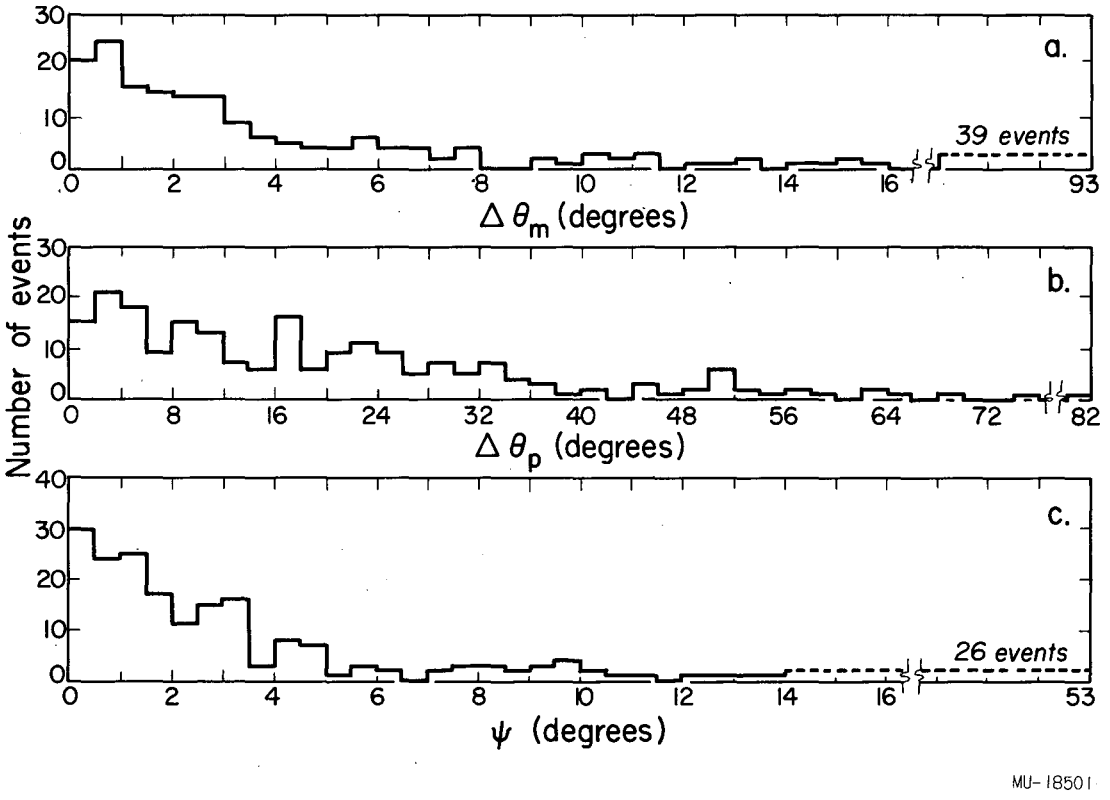

Fig. 21. Deviations of the scattering angles and coplanarity of background events from values expected for elastic scatters having the same proton ranges.

to 0.75 deg. A maximum error of 2.5 deg was then allowed on the measured value of the proton scattering angle. Many of the nonstopping protons left through the top or bottom glass of the chamber. Their average length in the chamber was thus $\sim$8 cm. From Fig. 17 it is seen that an error of 2.5 deg corresponds to $\sim$ 1.5 times the average error for elastic events having stopping protons.

In the transition region where some protons resulting from elastic scatters stop and some do not, it is possible that an acceptance criteria for nonstopping cases will either be too stringent or too relaxed. We tested the above criteria in the region 4 deg $\leq \theta_m \leq$ 5 deg by applying weighting factors to each event in which the proton stopped. These factors were calculated on the assumption of azimuthal symmetry around the incoming beam direction, and corrected for events in which the proton would hit one of the physical boundaries of the chamber. It was found that 29 events in the above interval would be expected to have nonstopping protons. In this interval, we counted 33 elastic events with nonstopping protons. This very good agreement means that our acceptance criteria for elastic events in which the protons did not stop were probably good.

Orientation of the Scattering Plane

The ability to detect an elastic event varies with the orientation of its scattering plane. Furthermore, at a particular orientation the detection efficiency decreases as the meson scattering angle decreases. This latter effect is most pronounced for scattering planes which are nearly vertical. Corrections for these two effects must be made to the observed data.

Figure 22 contains the folded azimuthal distributions of the elastic events. The azimuthal angle ϕ is that between the planes defined by tracks 0 and 1, and 0 and the vertical. The ranges for the meson scattering angle in the distributions were chosen so that approximately the same number of events appear in each distribution. Each distribution should be isotropic in ϕ, and the observed anisotropy is an indication of the number of events missed. Corrections C_ϕ, defined as the numbers by which the observed distributions must be multiplied to account for missed events, may be calculated from the figures. The values found in the two cases are $6.8 \text{ deg} \leq \theta^* \leq 13.3 \text{ deg}$, $C_\phi = 1.32 \pm 0.05$ and $13.3 \text{ deg} \leq \theta^* \leq 180 \text{ deg}$, $C_\phi = 1.16 \pm 0.02$. The elastic events found in each angular interval were multiplied by the appropriate factor.

Location of Events in the Chamber

Events with origins near the physical boundaries of the chamber will be lost if the outgoing particles leave the volume before making tracks of noticeable length. In this experiment, the fiducial volume was chosen so that the number of events that were lost because of passage of the tracks out the sides or ends of the chamber is considered negligible. Reference to Fig. 9 shows that the distance from the sides of the chamber to the boundaries of region B is $\sim$ 1 in. everywhere except near the four corners. Since only 3% of the events occurred within 2.5 cm of the top or bottom glass, a correction for events lost because of passage of the tracks out of one of these glasses is also unnecessary.

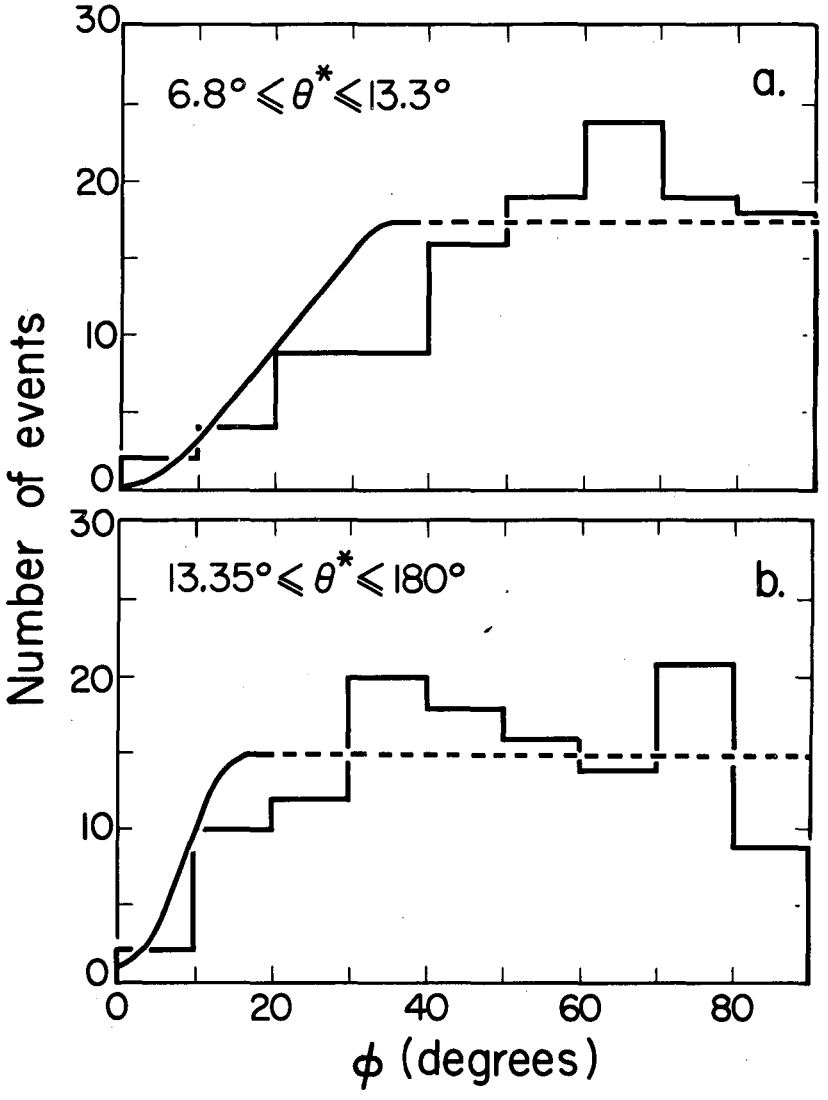

Fig. 22. Folded azimuthal distributions of elastic events.

Mu Contamination

The apparent path length traversed by the pions is somewhat less than the true path length because some of the tracks are made by muons and, to a smaller extent, electrons. The correction for contamination was calculated from beam geometry (Fig. 1), using a mean life of 2.56×10^{-8} sec for the pion and the average momentum of 5.17 Bev/c. It was found that 6% of the observed path length would be due to muons if all decay muons entered the chamber. The maximum decay angle, which is only ~ 0.3 deg, is insufficient to reduce significantly the number of muons entering the chamber. Muons produced ahead of the steering magnet, however, were rejected when their momenta were less than ~ 4.5 Bev/c . This fact reduces the figure above to $4 \pm (2)\%$. The error contains the uncertainty in the mean momentum of the pions.

Electrons in the chamber come from γ rays that originate at the target, in the magnets, and in the walls of the chamber. To a lesser extent, they also come from the decay of muons. During the scan, a search was made for bremsstrahlung. Under the assumption that we can detect an electron that loses 90% of its energy and that its total energy is very much greater than its rest energy, one calculates that the probability of an energy loss of this magnitude is 0.05.[19] No electrons were detected in the scan. The number present is of the order $2/0.05 = 40$. From the length in the chamber of 37 cm, which is applicable to noninteracting tracks, and the calculated track length of 12.22×10^5 cm, one finds that the contamination is $\lesssim 0.1\%$. A different calculation, based on the μ-e decay probability, showed that contamination from this source is only $\sim 0.04\%$. Clearly, electron contamination is negligible, and only the correction $C_\mu = 0.96 \pm 0.02$ need be multiplied by the observed path length in order to obtain the path length of the pions.

VII. RESULTS AND CONCLUSIONS

Angular Distribution

The uncorrected angular distribution in the center-of-mass system is plotted in Fig. 23. The sharp peak in the forward direction is characteristic of diffraction scattering, which is, without doubt, the dominant process at this energy. One also observes that no events were found in the backward hemisphere, a result that was reported earlier.[3] This fact is additional evidence for the diffraction nature of the elastic-scattering process at this energy. The events lying outside the central region of the pattern were selected as elastic on the basis of the previously stated criteria. Because of the small number of large-angle scatters, one must conclude that there is no conclusive evidence to support a description of the elastic interaction in terms of nondiffraction potential scattering.

The corrected angular distribution, represented in Fig. 24 by the encircled points, contains only the events whose meson scattering angles were ≥ 2 deg. The identification of elastic events was particularly difficult below this angle because the proton recoils are ≤ 0.7 cm. Multiple scattering and the shortness of the track frequently cause angle measurements to have abnormally large errors. In addition, many events are missed as one approaches the forward direction from 2 deg because the recoil is too short to be readily observable, if at all. The distribution in Fig. 23 was corrected by use of the basic equation,

$$\frac{d\sigma(\theta^*)}{d\Omega} = \frac{C_T}{L\rho} \frac{\Delta N}{\Delta \omega} \qquad (9)$$

where L is the calculated path length = 20.85 kilometers ±5%. This value was deduced from the path length measured in region A and the total number of events observed in regions A and B. In the interval $0.993 \geq \cos\theta^* \geq 0.833$, 210 events were observed in region A while 358 were found in region B. Here ρ is the number of free protons per cubic centimeter = $4.7 \times 10^{22} \pm 2\%$. This number depends on the density of expanded propane. The value used was 0.42 gms/cc (±2%). The number

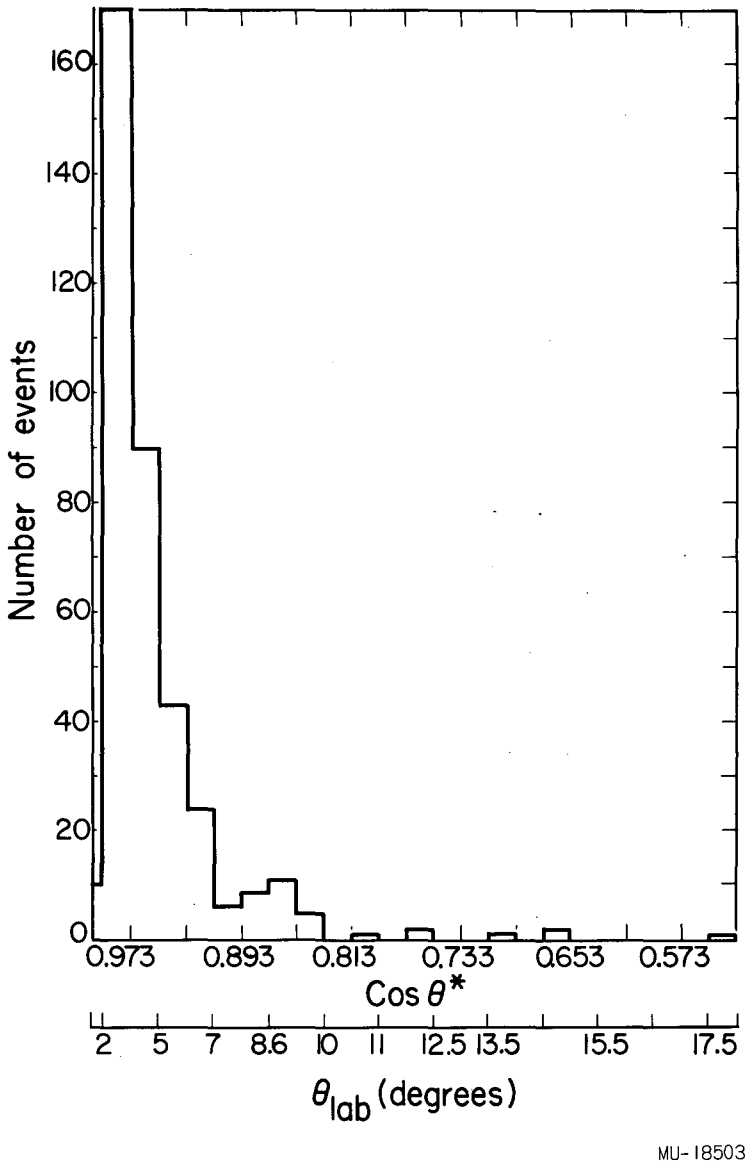

Fig. 23. Observed angular distribution of the elastic events.

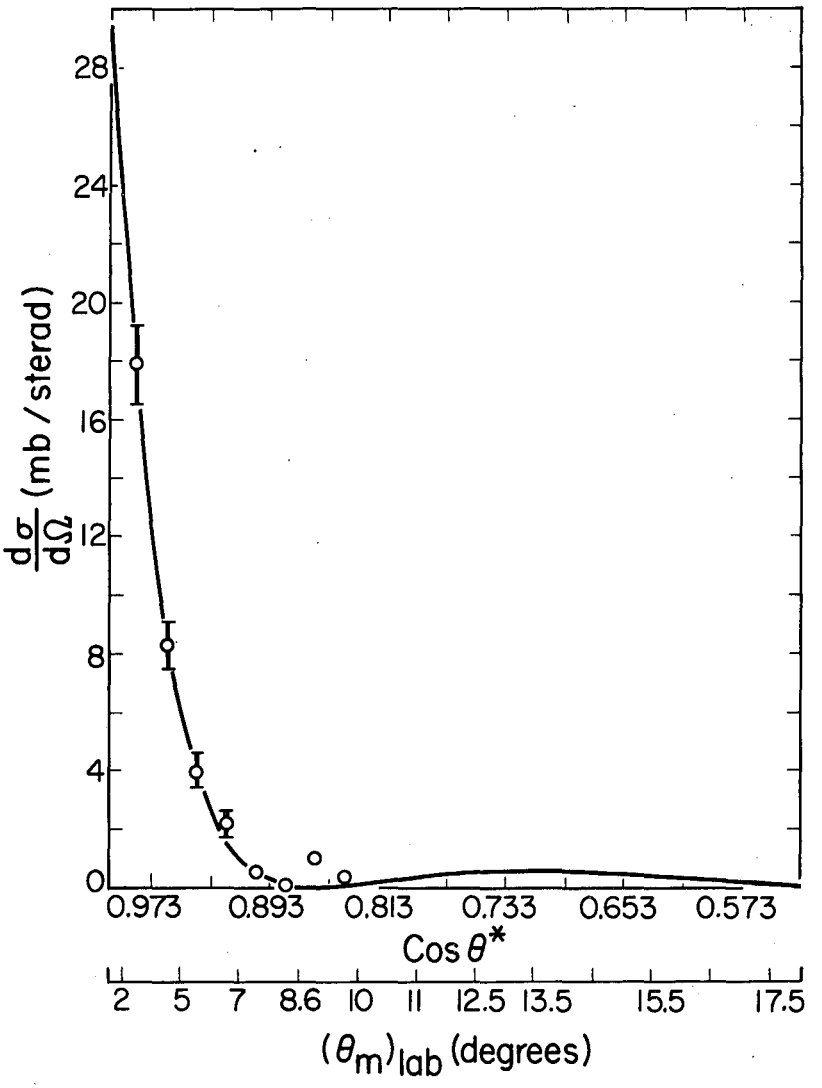

Fig. 24. The corrected angular distribution of the elastic events. The curve is that obtained when the nucleus is pictured as a "black" sphere.

of particles that scatter into the solid angle $\Delta\omega$ is ΔN, and C_T is defined in terms of the previously calculated corrections:

$$C_T = C_s C_b C_\phi / C_\mu \quad .$$

Two values of C_T were used. For $6.8 \text{ deg} \leq \theta^* \leq 13.3$ deg, we have $C_T = 1.30 \pm 5\%$, and for $13.3 \text{ deg} \leq \theta^* \leq 33.5$ deg, we have $C_T = 1.14 \pm 4\%$. Because of the above-mentioned identification difficulties, the formula was applied to only that portion of the distribution that lies in the interval $0.993 \geq \cos\theta^* \geq 0.833$.

In principle, the corrected distribution can be fitted by a cosine series, but the number of parameters that must be determined is prohibitively large. At 5 Bev one might expect angular-momentum states up to $\ell = 10$ to contribute. Furthermore, the observed distribution justifies the use of an optical model. The conventional model[20] was selected in which the elastic differential cross section is expressed in the form

$$\frac{d\sigma(\theta^*)}{d\Omega} = a \left| \frac{J_1(KR \sin\theta^*)}{KR \sin\theta^*} \right|^2 . \qquad (10)$$

The solid curve in Fig. 24 is a modified least-squares representation of the corrected data. Its equation is

$$\frac{d\sigma(\theta^*)}{d\Omega} = 1.19 \times 10^2 \left| \frac{J_1(7.78 \sin\theta^*)}{7.78 \sin\theta^*} \right|^2 \qquad (11)$$

A description of the procedure used to determine the most probable values of the constants in Eq. (11) is given in Appendix I.

The most salient features of the graph are seen to be its steep rise in the forward direction and its fairly rapid fall to zero. From Eq. (11) one calculates that the zero occurs for $\theta^* = 29.6$ deg and that we have $\frac{d\sigma(0)}{d\Omega} = 29.8 \pm 10\%$ mb/sterad in the center-of-mass system.

This value of the differential cross section in the forward direction can be compared with the value derived from the theoretical description of the scattering process.

When the elastic differential cross section consists of coherent and incoherent parts, it is described by the equation

$$\frac{d\sigma_{el}(\theta^*)}{d\Omega} = \left(\frac{d\sigma(\theta^*)}{d\Omega}\right)_C \pm \left(\frac{d\sigma(\theta^*)}{d\Omega}\right)_I , \qquad (12)$$

where the subscripts C and I stand for coherent and incoherent, respectively. In the forward direction the coherent part is given by

$$\frac{d\sigma_C(0)}{d\Omega} = \left| \text{Re } f_C(0) \right|^2 + \left| \text{Im } f_C(0) \right|^2 . \qquad (13)$$

Here Re and Im are the real and imaginary parts of the forward coherent scattering amplitude, f_C. In elastic π - p scattering, the only incoherent process is spin flip of the proton. It can be shown that the differential cross section for this process vanishes in the forward direction.[21] Therefore we have

$$\frac{d\sigma_{el}(0)}{d\Omega} = \left(\frac{d\sigma(0)}{d\Omega}\right)_C . \qquad (14)$$

The real part of the forward scattering amplitude, which is given by the dispersion relations,[22] is generally obtained by some method of numerical integration. To carry out the calculation requires a knowledge of the total π^- + p and π^+ + p cross sections at all energies. In particular, one needs quite reliable total-cross-section data in the vicinity of the energy under study, because one of the integrals becomes singular at the incident energy. Since total-cross-section data is rather incomplete for energies $\gtrsim$ 2 Bev, and the real part is expected to be small,[23] it was decided that the calculation of the real part would have no justification in this experiment. In accordance with the results of Cool et al,[23] we have assumed its contribution to be negligible at this energy.

The imaginary part is given by $\mathrm{Im}\, f_C(0) = K\sigma_T/4\pi$, where σ_T is the total cross section at 5 Bev and $K = 7.46 \times 10^{13}\ \mathrm{cm}^{-1} \pm 5\%$. The values obtained for $d\sigma_{el}(0)/d\Omega$ from all available information on σ_T are shown in Table II.

Table II

σ_T (mb)	Energy (Bev)	$\frac{d\sigma(0)}{d\Omega}$ (mb/sterad)	Reference
30	Extrapolated from lower energy data to 5.17 Bev	32	Cool et al[23]
22.5 ± 2.4	4.7	$18(\pm 12\%)$	Maenchen et al[3]
28.7 ± 2.6	4.3	$29.1(\pm 12\%)$	Wikner et al[24]
---	5.17	$29.8(\pm 10\%)$	This measurement

The errors in $d\sigma(0)/d\Omega$ are only those corresponding to the stated errors in σ_T. The value obtained in this work is seen to be in good agreement with that derived from the data of Wikner.[24]

The value of R, the pion-proton interaction radius, was found to be 1.04×10^{-13} cm $\pm 5\%$. The calculation was based on the previously stated value of K. The error is that resulting from the uncertainty in the mean beam momentum. As the value of the interaction radius depends on where the first zero of the Bessel function is taken when one fits the curve by trial and error, it is important that the observed distribution exhibit this point unambiguously. In our experiment the slight rise in the distribution in the interval $0.885 \trianglelefteq \cos\theta^* \trianglerighteq 0.861$ caused some uncertainty in the location of the zero. The modified least-squares procedure resulted in a value of R that did not directly involve the zero in its calculation. Following the initial calculation, a second was made in which the last four intervals of the observed distribution were

omitted. The statistical accuracy is seen to be very low in these intervals. The result was a value of $R = 1.05 \times 10^{-13}$ cm. The first zero of the Bessel function shifted to 29.3 deg. Evidently the omitted data do not contribute appreciably to the result.

The manner in which the interaction radius varies with energy, if indeed it does vary, is not known. Steinberger et al. obtained a value of $(1.08 \pm 0.06) \times 10^{-13}$ cm at 1.44 Bev,[2] while Maenchen et al. found the radius to be $(0.9 \pm 0.15) \times 10^{-13}$ cm at 5 Bev.[3] Recently Grishin et al. using Maenchen's data, calculated root-mean-square value of $(0.82 \pm 0.06) \times 10^{-13}$.[4] These results and the value derived in this experiment show no significant variations. One might conclude on this basis that there is substantially no change in the radius between 1 and 5 Bev, within experimental error. On the other hand, one wonders whether the lower values observed by Maenchen and by us are indicative of a decrease in this parameter with energy. The possibility that R changes with energy has been previously advanced.[7] Such a decrease might be explained crudely by assuming that only the first few angular-momentum states are important, even at high energies. While past attempts to describe the scattering have been made using only s through f waves,[25,26] primarily as a matter of convenience, it is not unreasonable to consider that this change in radius is an indication that higher waves are not involved.

The curve in Fig. 24 was continued beyond the first minimum to learn where the second maximum would be expected, if diffraction scattering continued to prevail at large angles. The pattern becomes very broad after the first zero, and the second peak occurs at $\sim$43 deg. The differential cross section is only $\sim$0.5 mb/sterad at this peak. These characteristics make the second peak, if it exists, very difficult to observe with these statistics.

Total Elastic Cross Section

In order to determine the total elastic cross section, the path length of the pions must be known. This was determined in the following way.

As previously stated, the number of tracks passing through region A of every tenth acceptable picture were counted. The positions of all origins of events on beam tracks were also recorded. The track length in the tenth picture was computed on the IBM 650, which was programmed under the assumption that all tracks traveled along the median plane of the chamber. The path length for noninteracting tracks is 37 cm at this height. The total track length is given by the expression $\sum_{L=1}^{955} 10x_i$, where x_i is the path length in each counted picture.

The calculated track length is 12.22×10^5 cm $\pm 2\%$. The error resulting from the assumption that all tracks pass along the median plane is considered negligible. The stated error above is due to the method used to compute the track length. The error in one of the terms is $\left| 10\, x_1 - \sum_{i=1}^{10} x_i \right|$. These errors for ten terms were found by calculating the actual path lengths in a series of pictures scattered throughout the film scanned. The standard error for any one term, σ, was found to be 8.19 meters. With a total of 955 terms, the fractional error in track length becomes $\frac{8.19 \times \sqrt{955}}{12.22 \times 10^3} = 2\%$.

The 227 events observed in region A were distributed as shown below:

Angular interval	No. of events
$1 \geq \cos\theta^* > 0.993$	10
$0.993 \geq \cos\theta^* > 0.973$	94
$0.973 \geq \cos\theta^* > 0.533$	123

(15)

The number of events in the first interval that were lost because of short recoils was estimated from Fig. 24. The shape of the curve represented by Eq. (10) in the forward direction depends rather critically on the product KR. The fairly large value of this product in

this experiment results in a curve that has a very narrow peak. The curve in the first interval can be approximated by a straight line. The average differential cross section in this interval is seen to be 26 mb/sterad. The number of events one would expect to observe is

$$N = 12.22 \times 10^{5} \times 4.7 \times 10^{22} \times 26 \times 10^{-27} \times 2\pi \times 7 \times 10^{-3} = 66 \pm 10. \tag{16}$$

Therefore, $\sim$ 56 events were missed in this interval. When the appropriate corrections have been applied to the events observed in the other intervals, one gets a total of 309 ± 22. The total elastic cross section is given by

$$\sigma_{el} = \frac{309}{12.22 \times 0.96 \times 10^{5} \times 4.7 \times 10^{22}} = 5.6 \pm 0.5 \text{ mb.} \tag{17}$$

The error consists of uncertainties in the corrected number of events (7%), corrected track length (3%), and density of expanded propane (2%). Using the constants in Eq. (11), one obtains $\sigma_{el} = 6.18$ mb.

The total elastic cross section is in agreement with that obtained by Maenchen et al, which is 4.7 ± 1 mb.[3] The value calculated by Grishin, et al. is 5 mb,[4] which also agrees with the above. The assumption that the proton acts like a totally absorbing sphere, however, results in a value $\pi R^2 = 34$ mb. With our extrapolated value of $d\sigma(0)/d\Omega$, the total hydrogen cross section becomes

$$\frac{4\pi \times 10^{-27} \sqrt{298}}{7.46} = 29.1 \text{ mb} \pm 10\% .$$

The opacity of the sphere is thus

$$\frac{(29.1 - 5.6) \times 10^{-1}}{\pi \times (1.04)^2} = 0.69 \pm 0.05.$$

ACKNOWLEDGMENTS

The Bevatron run from which these results have come was made with the cooperation of many individuals. Mr. Larry Oswald contributed greatly to the development of the chamber and to its successful operation at the accelerator. I should like to express my sincere appreciation to Larry and to the other members of the Cloud Chamber and Bevatron staffs who participated in the run.

Those who followed the analysis closely are:

Professor Wilson Powell upon whose suggestion the project was undertaken and under whose guidance it was performed. I take this opportunity to thank Dr. Powell very kindly for the advice and encouragement he has given me during our years of association.

Dr. William B. Fowler, Dr. Robert Birge, Mr. John I. Shonle, and Mr. Zaven G. Guiragossian who, through discussions with me, helped to clarify certain aspects of the work.

Mr. Howard S. White and his staff. Data reduction and programming for the IBM 650 were done by this group.

Miss Yuriko Hashimoto who rescanned the pictures.

APPENDIX

MODIFIED LEAST-SQUARES PROCEDURE FOR THE ANGULAR DISTRIBUTION

If the equation to be represented by a least-squares solution is nonlinear, the conventional method of calculating the unknown quantities is very difficult to carry out. The standard procedure that is used in such cases[27] will now be outlined for the specific case of the function

$$y = a\frac{J_1^2(b \sin \theta^*)}{(b \sin \theta^*)^2} \quad . \tag{18}$$

The differential cross section is y, and a and b are the quantities to be determined. Approximate values a_0 and b_0 must first be obtained. In this experiment we determined a_0 by equating the right-hand side of Eq. (12) to the measured differential cross section in the first five intervals, using the approximate value of $b \equiv KR \simeq 7.46 \times 10^{13} \times 10^{-13} = 7.46 = b_0$. The five values of a_i were averaged to obtain $a_0 = 1.03 \times 10^{-2}$ mb.

The differences $(\Delta y_i)'$ between the measured differential cross section and the value calculated from Eq. (11) above were then obtained in each of the eight intervals. The corresponding theoretical differences are given by the Taylor expansion:

$$(\Delta y_i)'' = \frac{\partial y}{\partial a_0} \Delta a_0 + \frac{\partial y}{\partial b_0} \Delta b_0 \quad . \tag{19}$$

The derivatives, evaluated by the use of the approximate values a_0 and b_0, are

$$\frac{\partial y}{\partial a_0} = \frac{J_1^2(b_0 \sin \theta^*)}{b_0^2 \sin^2 \theta^*} \quad , \tag{20}$$

$$\frac{\partial y}{\partial b_0} = 2a_0 \left\{ \frac{J_1(b_0 \sin \theta^*) b_0 \frac{dJ_1}{db_0} - J_1^2(b_0 \sin \theta^*)}{b_0^3 \sin^2 \theta^*} \right\}, \tag{21}$$

and

$$\frac{dJ_1}{db_0}(b_0 \sin\theta^*) = \sin\theta^* \left\{ J_0(b_0 \sin\theta^*) - \frac{J_1(b_0 \sin\theta^*)}{b_0 \sin\theta^*} \right\} \quad (22)$$

The functions J_0 and J_1 are tabulated.[28] The expression that was minimized is

$$(\Delta y_i)' - (\Delta y_i)'' . \quad (23)$$

By this procedure, Δa_0 in mb and Δb_0 were found to be

$$\Delta a_0 = 0.162 \times 10^2 \text{ mb}$$

and

$$\Delta b_0 = 0.318 .$$

REFERENCES

1. Lattes, Occialini, and Powell, Nature 160, 453 (1947).
2. Chretien, Leitner, Samios, Schwartz, and Steinberger, Phys. Rev. 108, 383 (1957).
3. Maenchen, Fowler, Powell, and Wright, Phys. Rev. 108, 850 (1957).
4. Blokhintsev, Barashenkov, and Grishin, Soviet Physics (JETP) 8(35), 215 (1959).
5. A. P. Batson and L. Riddiford, Proc. Roy. Soc. (London) A, 237, 175 (1956).
6. Chen, Leavitt, and Shapiro, Phys. Rev. 103, 211 (1956).
7. Fowler, Shutt, Thorndike, and Whittemore, Phys. Rev. 103, 1489 (1956).
8. Robert Hofstadter, Revs. Modern Phys. 28, 214 (1956).
9. See, for example, J. M. Blatt and V. F. Weisskopf, Theoretical Nuclear Physics, Chapter VIII (Wiley,and Sons Co., New York, 1952).
10. Fowler, Shutt, Thorndike, and Whittemore, Phys. Rev. 93, 861 (1954).
11. Donald A. Glaser, Phys. Rev. 9, 762 (1953).
12. David Hotz, The Production of Neutral Hyperons by 5-Bev π^- Mesons (Thesis), UCRL-8715, April 13, 1959.
13. Fowler, Powell, and Shonle, Nuovo cimento 11, 428 (1959).
14. Powell, Fowler, and Oswald, Rev. Sci. Instr. 29, 874 (1958).
15. Robert W. Birge, LRL Engineering Note Bev-306, Feb. 3, 1958.
16. L. Baggett, Pi-P Elastic Scattering and Single Pion Production at 0.939 Bev/c, UCRL-8302, May 28, 1958.
17. G. Clark and Diehl, Range-Energy Relation for Liquid-Hydrogen Bubble Chambers (M. S. Thesis), UCRL-3789, May 1957.
18. Frank Solmitz, LRL Engineering Note 4320-60 M6, November 21, 1957.
19. John Shonle, Lawrence Radiation Laboratory, private communication.
20. Fernbach, Serber, and Taylor, Phys. Rev. 75, 1352 (1949).
21. Jack Leitner, π^--P Elastic Scattering at 1.44 Bev, NEVIS-28, January 1957, the corresponding publication is reference 2, above.

22. M. L. Goldberger, Phys. Rev. 99, 979 (1955).
23. Cool, Clark, and Piccioni, Phys. Rev. 103, 1082 (1956).
24. Frederick Wikner, Nuclear Cross Sections for 4.2-Bev Negative Pions (Thesis), UCRL-3639, January 1957.
25. Walker, Hushfar, and Shepard, Phys. Rev. 104, 526 (1956).
26. A. Erwin and J. Kopp, Phys. Rev. 109, 1364 (1958).
27. A. G. Worthing and J. Geffner, Treatment of Experimental Data, Chapter XI (Wiley and Sons Co. New York, 1943).
28. E. Jahnke and F. Emde, Tables of Functions with Formulae and Curves, Section VIII (Dover Publications, New York, 1953).